AD-A072 180 SUSSEX UNIV BRIGHTON (ENGLAND) SCHOOL OF ENGINEERING--ETC F/G 11/6
RESEARCHES ON ALLOYS RAPIDLY QUENCHED FROM THE MELT.(U)
1978 R W CAHN, B CANTOR, M G SCOTT N00014-78-G-0048

UNCLASSIFIED NL

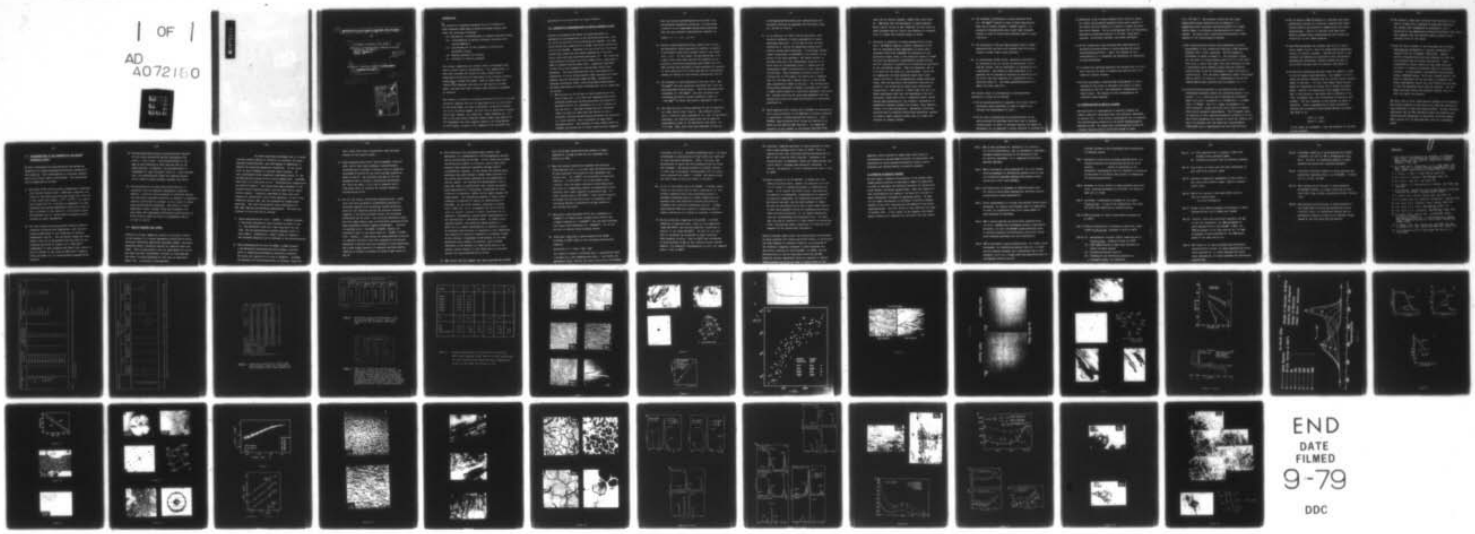

END
DATE
FILMED
9-79
DDC

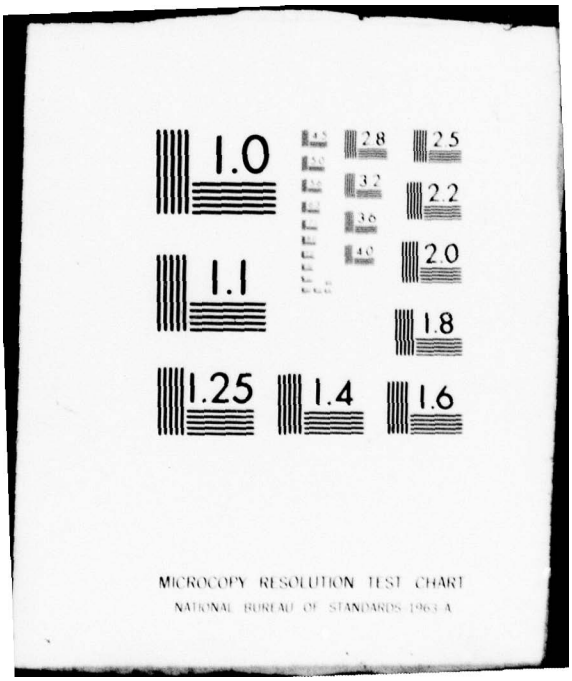
1.0
1.1
1.25
1.4
1.6
1.8
2.0
2.2
2.5
2.8
3.2
3.6
4.0
MICROCOPY RESOLUTION TEST CHART
NATIONAL BUREAU OF STANDARDS 1963-A

(6) RESEARCHES ON ALLOYS RAPIDLY QUENCHED FROM THE MELT.

by

(10) R.W./Cahn, B./Cantor, M.G./Scott

School of Engineering & Applied Sciences,
University of Sussex,
~~Falmer~~, Brighton,
Sussex, UK.

411313

(9) 1st annual technical report no. 1, on grant number

(15) N-00014-78-G-0048

(12) 52p.

(11) 1978

INTRODUCTION

The scientific programme sponsored by the U S Office of Naval Research (ONR) grant N-00014-78-G-0048 covered work under the following 5 headings:

(a) Martensitic transformations in rapidly quenched alloys;

(b) Investigations on metallic glasses (structure and crystallisation);

(c) Transformations in and strength of non-ferrous metastable alloys;

(d) Rapidly quenched tool steels;

(e) Diffusion in metallic glasses.

This report summarises our current state of knowledge about each of these areas of investigation. For completeness, we have also included the results of some closely-related experiments which were not described in the original research proposal for N-00014-78-G-0048. Some of these additional results were obtained just prior to the start of the ONR grant, and some have been obtained under parallel programmes of research.

The research concerned with rapidly quenched tool steels (d) is now virtually complete and will be described fully in this report. On the other hand, our work on diffusion in metallic glasses (e) is in its early stages, and will not be described in detail until later reports are submitted. Under headings (a), (b) and (c) we have fairly complete results about some aspects of the programme, but other aspects remain to be investigated; in this report, we give a full summary of our available data

and describe our priorities for future studies.

(a) MARTENSITIC TRANSFORMATIONS IN RAPIDLY QUENCHED ALLOYS

We have investigated the effect of splat-quenching on martensitic transformations in the following materials: pure Fe, Fe-Ni alloys with 5,10,15,20,25,30 and 40wt%Ni, the same Fe-Ni alloys with additions of 0.1wt%C, and Fe-Mn alloys with 5,10,15 and 20wt%Mn. Specimens of each alloy were levitation melted under argon and then splat-quenched by a 2-piston device which has been described previously (1). The resulting splat-quenched specimens were disc-shaped foils, approximately 20mm in diameter and 50-100μm thick. Comparison specimens of each alloy were prepared by conventional solid state quenching. The resulting materials were investigated by a combination of X-ray diffractometry (XRD) scanning and transmission electron microscopy (SEM and TEM), differential scanning calorimetry (DSC), and microhardness measurements. The main conclusions of these investigations can be summarised as follows:

1) SEM pictures of the surface of splat-quenched pure Fe foils (figs 1(a) - (c)) show that depending upon splat-quenching conditions the microstructure can consist of equiaxed ferrite (α), martensite (α'), of a mixture of the two (α/α'). Sections through the foil thickness (figs 1(d) and (e)) show that the ferrite is not a retained δ-ferrite solidification structure (as described in a later section, this is possible in some splat-quenched steels). The presence of only slight traces of columnar solidification on these cross-sections suggests

that the ferrite and martensite do not form in an as-solidified austenitic structure, in other words δ-ferrite is not suppressed during splat-quenching. Thus the most probable transformation sequence is:

liquid → δ → γ → α,α', or α/α'

2) Ferritic splat-quenched Fe has a grain size of ∿4μm and martensitic splat-quenched Fe consists of packets of martensite laths with a packet size of ∿4μm (figs 1(a) - (c)). In both cases, the microstructure is on a much finer scale than ferritic Fe produced by conventional solid-state quenching from ∿1200K (fig 1(f). TEM confirms that martensitic splat-quenched Fe consists of laths which are ∿0.1-0.3μm wide and are occasionally though not always in twin-related orientations (fig 2).

3) The hardness of splat-quenched Fe can vary from ∿ 250-700 $Kgmm^{-2}$ and this variation correlates well with the splat-quenched microstructure. Ferritic specimens have a hardness of ∿ 250 $Kgmm^{-2}$, and this increases with increasing martensite content reaching a value of ∿ 700 $Kgmm^{-2}$ in wholly martensitic specimens (table 1).

4) The high hardness of splat-quenched Fe can be explained as a Hall-Petch effect (fig 3). The effective grain size of ferritic splat-quenched Fe is ∿ 4μm; in martensitic specimens, the effective grain size can be taken as approximately equal to the martensite lath width, i.e. 0.1-0.3μm. Then, data from splat-quenched Fe fits on

an extrapolated Hall-Petch plot obtained from conventional ferritic Fe specimens (2) with grain sizes of $\sim$ 50-100 μm (fig.3).

5) It is difficult to relate the microstructure (and therefore hardness) of splat-quenched Fe to splat-quenching conditions. To try and do this, we have constructed a device for measuring cooling rates directly during splat-quenching. A fine gauge chromel-alumel thermocouple is embedded on the surface of one piston in the splat-quencher, the piston surface is polished down until the thermocouple junction is no wider than the thermocouple wires ($\sim$ 100μm) and the thermocouple signal is monitored on a fast time-base oscilloscope. When extraneous electrical noise is filtered out of the signal, the system has a response time of 0.3-0.4ms and a typical cooling curve during splat-quenching is shown in fig 4(a). The cooling rate during splat-quenching is found to increase with either a higher piston speed or a lower melt superheat (fig 4(b)). The cooling curves do not give good agreement with the predictions of Bletry's heat-flow analysis of two-piston quenching (3).

6) Splat-quenched Fe-Ni alloys with $\overset{\sim}{<}$ 22wt%Ni are martensitic with a microstructure in the SEM which is almost identical to martensite in splat-quenched Fe (fig 5(a)). With $\overset{\sim}{>}$ 22wt%Ni, splat-quenched Fe-Ni alloys are austenitic as shown by both XRD and SEM (fig 5(b)). By comparison, austenite is not present in solid-state quenched Fe-Ni

until the Ni content exceeds ∿ 30wt% (fig 5 and table 2). TEM shows that the martensite in splat-quenched Fe-Ni (fig 6) is not in fact identical to that found in splat-quenched pure Fe (fig 2) and consists of extremely thin (∿ 0.02μm) twin-related plates or laths.

7) Retention of austenite in splat-quenched Fe-Ni alloys with ∿ 22-30%wtNi implies a drastic depression of Ms. This is confirmed by DSC experiments in which splat-quenched alloys with 5-20wt%Ni are annealed for progressively longer times in the austenite region at 1000K, and both the martensite transformation during cooling and the reversion to austenite on re-heating are monitored by the calorimeter output. When the annealing time is very short (of the order of a few seconds), the Ms and As temperature are both depressed below their usual values (fig 7(a)). With progressively longer annealing times, both the martensite and austenite reactions are modified, and the Ms and As reach their conventional values after ∿ 1000 mins at ∿ 1000K (figs 7(b) and (c)). These experiments show that the depression of Ms has a structural origin and is not a transitory effect caused during splat-quenching by, for instance, deformation or hydrostatic pressure between the pistons, stray magnetic fields, or a high cooling rate. Martensite nucleation kinetics must be modified during splat-quenching, because of either a small austenite grain size or a small dislocation or vacancy content.

8) The hardness of martensite in splat-quenched Fe-Ni is $\sim$ 700 $Kgmm^{-2}$ similar to that in splat-quenched Fe. When the Ni content exceeds $\sim$ 22wt%Ni however, the austenitic microstructure has a much lower hardness, similar to that in solid-state quenched high Ni alloys (fig 8(a)).

9) The depression of Ms and high hardness found in splat-quenched Fe-Ni are both still present when the alloys contain 0.1wt%C (table 2 and fig 8(b)).

10) In conventional Fe-Mn alloys, austenite transforms to bcc martensite only at low Mn concentrations; with a high Mn content, the bcc martensite is replaced by hcp ε-martensite. The effect of splat-quenching is to suppress the bcc martensite reaction as described above for Fe-Ni, but the formation of ε martensite is not affected (table 2). The splat-quenched martensite is again very hard (fig 8(c)).

Our current lines of investigation on splat-quenched martensitic alloys are as follows:

1) We are modifying Bletry's analysis (3) of heat flow in two-piston splat-quenching in order to explain our cooling rate measurements in fig.4.

2) We are also investigating the microstructures of the splat-quenched Fe specimens which were used to measure cooling rates, in order to determine whether the amount of martensite is, as expected, a direct function of cooling rate.

3) Depression of M_S in splat-quenched Fe-Ni could be caused by a small as-solidified austenite grain size, similar to the effect seen by Turnbull and Cech(4) in small particle-size Fe-Ni powders. We are investigating this by determining martensite nucleation kinetics in the DSC, using splat-quenched, solid-state quenched, and powder specimens.

4) We are conducting a more detailed TEM investigation of martensite microstructures in splat-quenched and splat-quenched/annealed Fe-Ni. Again, the purpose of this investigation is to determine why martensite is suppressed by splat-quenching.

5) A vacuum melt-spinning apparatus has already been partially built and will be used to produce melt-spun Fe and Fe-Ni tapes for tensile testing.

6) We have performed a detailed TEM investigation of splat-quenched Zr-Nb alloys to determine the effect of splat-quenching on the bcc → hcp martensite transformation in these alloys. The results of this investigation are currently being analysed.

(b) INVESTIGATIONS ON METALLIC GLASSES

Our main areas of investigation of metallic glasses are thermal stability (described here) and diffusion (described in section (e)). In an earlier investigation (5) we reported the crystallisation kinetics of the glass $Fe_{40}Ni_{40}P_{14}B_6$ as measured by DSC. We showed that crystallisation occured by a single reaction with an activation energy of about

3.9×10^5 $Jmol^{-1}$. The kinetics fitted the well known Johnson-Mehl-Avrami equation with an exponent $n \sim 4$, suggesting either interface controlled growth of a single crystal phase, or diffusion limited growth of a eutectic product. We report here a detailed microstructural investigation of the crystallisation process.

1) The crystallisation kinetics were determined by direct measurements of the crystalline fraction in TEM specimens prepared after "bulk" annealing. The TTT diagram so determined is shown in Figure 9. The activation energy for the onset of crystallisation was $4.3 \pm 0.1 \times 10^5$ $Jmol^{-1}$. This value is about 10% larger than that determined by DSC, a discrepancy which probably arises from the different sensitivities of the two techniques to small fractions of crystallinity. Over the whole temperature range investigated (320 to 400°C) the kinetics of transformation fitted the Johnson-Mehl-Avrami equation with an exponent of $n \sim 4$.

2) X-ray diffraction patterns of the partially and fully transformed specimens showed two crystalline phases to be present, f.c.c. austenite and a body-centred tetragonal phase with lattice parameters a = 0.885nm and c = 0.440nm (both ± 0.005nm). The f.c.c. phase is presumed to be Fe-Ni austenite, though the Fe:Ni ratio cannot be deduced from lattice parameter measurements. The tetragonal phase is identical to that reported previously by Walter et al (6). The lattice parameters are similar to those for $(FeNi)_3$ P(7) and it is probable that the phase has a stoichiometry $(FeNi)_3(PB)$ and is isomorphous with both Fe_3P and Ni_3P.

3) Fig 10 shows an SEM micrograph of a polished and etched longitudinal section of a partially crystallised ribbon. Crystallisation has occured at random within the ribbon cross-section. This is in contrast with some other metallic glasses where crystallisation has occured preferentially on the ribbon surfaces.

4) From TEM micrographs the crystals were shown to have a barrel shape (fig.11), and a two phase lamellar appearance typical of eutectic crystals. Towards the centre of the crystals the lamellae are oriented in only two mutually perpendicular directions, whereas towards the edge of the crystal sections they lie radially (fig.12(a)(b)).

5) All electron diffraction patterns could be indexed in terms of the two phases described above. For example fig.12(c) shows the pattern obtained from the circular crystal section shown in fig.12(a). At first this simple square pattern might be interpreted as arising from a single tetragonal phase. However, by forming dark field images from each spot in the pattern it was shown that in addition to the <001> tetragonal zone, two orientations of austenite were present. The full indexing of this pattern is shown in fig.12(d). From a consideration of other diffraction patterns the orientation relationship between the phases was shown to be:

$$\langle 110\rangle_T \parallel \langle 110\rangle_\gamma$$
$$\langle 001\rangle_T \parallel \langle 112\rangle_\gamma$$

In all cases the tetragonal c axis was parallel to the axis of the crystals.

6) The austenite phase also contained fine structure in the form of fringes with a spacing of about 5nm (fig.13(a)). The fringes were accompanied by streaking in $\langle 111 \rangle_\gamma$ directions of the appropriate diffraction patterns (fig.13(b)). This suggests that the austenite phase contains either stacking faults or fine twins.

7) From the above evidence it was concluded that the glass $Fe_{40}Ni_{40}P_{14}B_6$ decomposed by a eutectic mechanism into austenite and the tetragonal $(FeNi)_3(PB)$. Similar eutectic decompositions have been observed in other metallic glasses such as Fe-B(8) and Pd-Si(9). Such a transformation should require no long range diffusion and hence no composition gradient ahead of the growing crystals. As confirmation, microanalysis was performed using a STEM/EDX system. With such a system analysis for boron is impossible but we were able to establish that within experimental limits the ratio Fe:Ni:P was the same in both the amorphous matrix and the crystals. The two phase structure within the crystals, however, was on a scale too small for analysis.

The above work on Fe-Ni based metallic glasses is now complete. Our current research in this area is to study the crystallisation behaviour of some metal-metal glasses. We have obtained preliminary DSC and TEM information about the stability and crystallisation mechanisms in some Zr-Ni and Zr-Fe glasses. These results will be described more fully in a subsequent report.

(c) TRANSFORMATIONS IN AND STRENGTHS OF NON-FERROUS METASTABLE ALLOYS

We have investigated the microstructure and mechanical properties of rapidly-quenched Pb-Sn eutectic prepared by melt-spinning. This investigation is virtually complete, and little further work is anticipated. The conclusions can be summarised as follows:

1) Melt-spun Pb-Sn eutectic exhibits superplastic behaviour, with failure strains often > 100% and a sigmoidal variation of log flow stress with log strain rate (fig 14). In the strain rate region $\sim 10^{-5} - 10^{-3} s^{-1}$, the strain rate sensitivity is ~ 0.42 and is independent of tape thickness and testing temperature (fig 14 and table 3). This is similar to the value of ~ 0.48 found by Avery and Backofen (10) in Pb-Sn eutectic prepared conventionally by heavy deformation.

2) The flow stress of melt-spun Pb-Sn eutectic shows an Arrhenius variation with temperature, with log flow stress proportional to the reciprocal of absolute temperature (fig 15). The activation energy for superplastic flow can be determined from the slope of the Arrhenius plots and is found to be ~ 54KJ mole^{-1} independent of tape thickness and strain rate (table 4). This is similar to the value of 48KJ mole^{-1} found by Cline and Alden (11) in conventionally prepared Pb-Sn eutectic.

3) The melt-spun Pb-Sn eutectic microstructure consists of fine scale equiaxed Pb and Sn rich grains (fig 16(a)), ~ 4μm in size. This microstructure is the same on both surfaces of each tape and also on the cross-sections; in addition, the microstructure is independent of tape thickness (table 5). After deformation, the microstructure shows the expected surface relief caused by grain-boundary sliding (fig 16(b)).

4) The microstructure of melt-spun Pb-Sn eutectic is consistent with the observed superplastic behaviour. However, it has not proved possible to determine whether the fine-scale two-phase structure is caused by a degenerate eutectic solidification process, or as a result of rapid post-solidification coarsening. The latter of these seems more likely, because Cline and Livingston (12) have shown that high-speed directional solidification of Pb-Sn eutectic does not lead to a morphology similar to that in fig 16.

(d) RAPIDLY QUENCHED TOOL STEELS

Production of many commercial alloys is critically limited by the presence of a coarse segregated solidification microstructure containing undesirable secondary phases, and rapid quenching offers a potential method for removing these problems. This is particularly true for high-speed tool steels and there has been considerable interest in investigating the effect of splat-quenching on this type of high-alloy steel (13). In previous investigations,

the splat-quenching techniques led to a rather variable product making it difficult to interpret the splat-quenched microstructures, and also making it impossible to measure the resulting mechanical properties. In our recent work, we have attempted to overcome these problems. We have investigated three commercial high-speed steels, T1, M2 and M42 and six ternary Fe-W-C alloys ranging from 6-23wt%W, each with a 2:1 atom ratio of W:C. Detailed alloy compositions are given in table 6. The alloys were splat-quenched in the 2-piston device described above, and this gave fairly reproducible results. Comparison specimens of each alloy were prepared by conventional solid state quenching and one of the commercial steels, M42, was also prepared by plasma-spray-quenching. The resulting materials were investigated by XRD, SEM, TEM and microhardness measurements. The main conclusions of this work are as follows:

1) Splat-quenching Fe-W-C with < 13wt%W, < 0.42wt%C produces a fine-scale martensitic lath structure as shown in fig 17. The martensite laths are 1-3μm long and 0.2-0.3μm wide, and the misorientation between adjacent laths is quite small. Occasionally, slight traces of cementite and retained austenite can be detected in the microstructure.

2) Splat-quenching Fe-W-C with 16.5wt%W, 0.5wt%C produces a solidification microstructure with primary δ-ferrite cells or dendrites surrounded by peritectic austenite. The cells are typically 0.6-1.0μm in diameter. Although the majority of the microstructure is cellular, there are

small areas which have a martensitic lath structure similar to the lower W alloys.

3) Splat-quenching both Fe-W-C with 20-23wt%W, 0.65-0.75 wt%C, and T1 tool steel produces a solidification microstructure of primary δ-ferrite cells or dendrites surrounded by peritectic austenite and M_6C carbide as shown in fig 18. The austenite and M_6C in the cell boundaries show a variable orientation relationship. The cells are again ∿ 0.6-1.0μm in diameter and in some areas there is evidence for primary austenite solidification cells.

4) For all the alloys, solid-state quenching from ∿ 1400K into iced brine produces a predominantly martensitic structure together with coarse M_6C carbide particles which are not dissolved during the solution treatment. Compared to the splat-quenched alloys, the following differences can be noted. The low alloy martensite laths are 5-10 times smaller than in solid-state quenched alloys. Splat quenching produces complete metastable solution of carbides up to > 16.5wt%W, 0.54wt%C, whereas the solubility limit in the solid state is ∿ 10wt%W. 0.3wt%C (14). Finally, in high alloys the splat-quenched structure is radically different from that produced by solid-state quenching; δ-ferrite cells are retained to room temperature, and a much larger quantity of austenite and much smaller quantity of carbide is present as shown by XRD traces in fig 19.

5) The transition with increasing alloy content from martensite to a predominantly δ-ferrite/austenite mixture can be rationalised as follows. In all alloys the primary solidification product is δ-ferrite, and at high alloy contents some peritectic austenite and M_6C form in interdendritic regions. As the alloys cool during splat-quenching they pass through a region where austenite is the stable phase before reaching the low-temperature α-ferrite region. Our cooling rate measurements (fig 4) show that there is insufficient time during two-piston splat-quenching for a diffusional transformation from δ-ferrite to austenite, before ferrite again becomes the stable phase. The alternative massive or shear transformation is expected to require an undercooling of ∿ 200-300K. At low alloy contents, austenite is stable over ∿ 600K (14) so it is possible for the δ-ferrite cells to undergo a massive or shear transformation to austenite, followed by a second shear transformation to the conventional α' martensite laths. At higher alloy contents however, the austenite region narrows to ∿ 200K (14) so a shear transformation to austenite cannot be nucleated and δ-ferrite is retained to room temperature. The retention of peritectic austenite is probably caused by two effects; a depression of Ms because of the high metastable alloy content in solution, and a further depression of Ms because of a small grain size or low vacancy content similar to that described in a previous section for splat-quenched Fe-Ni alloys.

6) XRD traces (fig 19) suggest that splat-quenched M2 and M42

tool steels have microstructures similar to splat-quenched T1, though we have not yet confirmed this directly by TEM.

7) When the present results are compared with previous investigations (13), it is clear that the microstructure of splat-quenched tool steels is very dependent upon cooling rate. At $\sim 10^8 Ks^{-1}$ the structure is completely δ-ferrite. At 10^6-$10^7 Ks^{-1}$, as in the present work, δ-ferrite cells are again retained to room temperature but there is a significant amount of retained peritectic austenite and a small quantity of peritectic M_6C. At lower cooling rates $\lesssim 10^4$-$10^5 Ks^{-1}$, very little δ-ferrite is present and the microstructure is austenitic with increasing amounts of martensite and M_6C carbide as the cooling rate falls.

8) Martensitic splat-quenched Fe-W-C has a hardness of $\sim$ $700 Kgmm^{-2}$; at higher alloy contents the δ-ferrite has a higher hardness of $\sim 1050 Kgmm^{-2}$; and the splat-quenched tool steels have hardnesses of $\sim 800 Kgmm^{-2}$. We are not yet able to explain these hardness values.

9) Isothermal tempering of splat-quenched Fe-6.3wt%W - 0.21wt%C at 600°C leads to the following precipitation sequence:

martensite (α') → Fe_3C → W_2C → M_6C

The cementite causes a softening when it precipitates after $\sim$ 40 mins as a fine Widmanstatten distribution within the martensite laths, obeying the usual orientation relationship

(fig 20(a) and (b)). Secondary hardening after ∿ 2½ hours corresponds to precipitation of W_2C within the laths and at lath and grain boundaries. After ∿ 50 hours, M_6C precipitates at grain and lath boundaries and the alloy has overaged. The ageing sequence is broadly similar to that seen by Davenport and Honeycombe (15) in solid-state quenched Fe-6.3wt%W - 0.21wt%C, and ageing curves for both types of alloy are shown in fig 20(c).

10) In all 3 tool steels and in Fe-23wt%W - 0.75wt%C (essentially T1 tool steel with Cr and V replaced by W), isochronal tempering after splat-quenching produces a secondary hardening peak at a higher temperature and hardness than that obtained by conventional solution treatment and solid-state quenching (fig 21). Plasma-spray-quenched M42 also exhibits a hardening peak at higher temperature but without an increase in hardness.

11) During isochronal tempering of Fe-23wt%W - 0.75wt%C, cementite is detected after 1 hour in the temperature range 300-550°C, and retained austenite transforms to ferrite in the range 550-600°C. We have not yet been able to establish the mechanism of these reactions. Peak hardness is after 1 hour at 650°C and corresponds to precipitation of M_6C in the δ-ferrite cells (fig.22). However, the austenite transformation is still not complete after 1 hour at 650°C.

12) Isochronal tempered specimens of splat-quenched T1 steel show a peak hardness after ∿1hour at 650°C, which is associated with very fine-scale mottled precipitation of W_2C in the δ-ferrite cells (fig.23). Otherwise, the microstructure is remarkably stable and tempering has very little effect; although some austenite transforms to ferrite, the majority is still retained even after 1 hour at 650°C.

13) Splat-quenched T1 and Fe-23wt%W - 0.75wt%C have very similar microstructures, however the presence of Cr and V in T1 leads to a marked difference in tempering response. In T1 (unlike the Fe-W-C alloy), precipitation of cementite is suppressed, transformation of austenite is partially suppressed, the hardening precipitate is W_2C rather than M_6C, and the peak hardness is higher. We have not determined how Cr and V cause these effects. In both splat-quenched alloys the hardening precipitate forms with more difficulty, ie. at higher temperature, than the corresponding solid-quenched alloy. We think that this may be related to a lower density of nucleating sites (dislocations and/or vacancies) in δ-ferrite cells compared to the conventional martensite.

Several problems remain about the microstructure and hardness of splat-quenched tool steels and Fe-W-C alloys, in particular the high hardness of retained δ-ferrite, the mechanism of the different tempering responses in splat-quenched and solid-state quenched T1 and Fe-23wt%W - 0.75wt%C, and the microstructure of the Mo high-speed steels M2 and M42. Extensive further experiments would be required to resolve these problems and we do not plan to pursue these in the

immediate future because we regard some other areas of investigation as having higher priority (in particular, the experiments on splat-quenched martensitic alloys, and on diffusion and crystallisation of metallic glasses).

e) DIFFUSION IN METALLIC GLASSES

We have begun a computer investigation of the Bernal dense random packed structure by devising a number of algorithms in order to determine the detailed structure of interstitial sites between the Bernal packed atoms. When the results of this investigation are complete, the data will be used to model diffusional processes in amorphous metals. We have not yet begun experiments on *diffusion* in metallic glasses because we are still awaiting two new members of our splat-quenching group - one will arrive in June 1979 and the other in October 1979. A full report of the computer and experimental studies will therefore be left until the next report.

Fig.1 SEM of splat-quenched Fe: surfaces of (a) ferritic, (b) ferritic/martensitic, and (c) martensitic specimens; through-thickness sections of (d) martensitic and (e) ferritic specimens; (f) a comparison solid-state quenched specimen.

Fig.2 TEM of martensitic splat-quenched Fe: (a) & (b) bright-field micrographs (c) diffraction pattern from (b) and (d) diffraction analysis showing twin-related orientations and a {112} lath boundary.

Fig.3 Hall-Petch plot of hardness vs effective grain size for ferritic solid-state quenched Fe, and both ferritic and martensitic splat-quenched Fe.

Fig.4 Direct measurements of cooling rate during 2-piston splat-quenching: (a) typical oscilloscope trace of temperature vs time; (b) accumulated data for a large number of splat-quenched Fe specimens.

Fig.5 SEM of splat-quenched and solid-state quenched Fe-Ni: (a) with < 22wt%Ni both techniques produce a martensitic structure; (b) with ∿22-30wt%Ni splat-quenching leads to retained austenite solidification cells while solid-state quenched specimens are still martensitic.

Fig.6 TEM of martensitic splat-quenched Fe-Ni: (a) bright field micrograph; (b) diffraction pattern from (a); (c) diffraction analysis showing twin orientations and a {112} boundary; (d) & (e) a bright-field and dark-field pair of micrographs showing contrast

reversal because of the alternating twin orientations of adjacent plates.

Fig 7 Depression of Ms and As in splat-quenched Fe-Ni: (a) as-splat-quenched and conventional Ms and As vs Ni content; effect of annealing on (b) martensite transformation and (c) reversion to austenite as monitored in the DSC by heat output vs temperature for splat-quenched Fe-Ni.

Fig 8 Hardness vs alloy content in splat-quenched and solid-state quenched specimens of (a) Fe-Ni, (b) Fe-Ni-0.1 wt%C and (c) Fe-Mn.

Fig 9 Isothermal transformation diagram for the glass $Fe_{40}Ni_{40}P_{14}B_6$. ts and tf are respectively the times for start and completion of crystallisation.

Fig 10 SEM micrograph of ribbon cross-section annealed 3h at 365°C.

Fig 11 Typical distribution of crystals in partially transformed $Fe_{40}Ni_{40}P_{14}B_6$. Annealed 11 mins at 385°C.

Fig 12 (a) Approximately circular {001}T cross-section in $Fe_{40}Ni_{40}P_{14}B_6$. Annealed 42 mins at 372°C

(b) High magnification to show fine structure at centre of above crystal

(c) Diffraction pattern from (a)

(d) Indexing of the diffraction pattern (c), • tetragonal phase, ∘,▫ austenite.

Fig 13 (a) High magnification of crystal to show fine fringes within austenite phase
(b) Diffraction pattern from (a) showing streaking.

Fig 14 Flow stress vs strain rate for nine thicknesses of melt-spun Pb-Sn eutectic tapes.

Fig 15 Arrhenius temperature dependence of flow stress in melt spun Pb-Sn eutectic tapes, tested at several strain rates.

Fig 16 SEM of the surface of melt-spun Pb-Sn eutectic tape (a) as-melt-spun;
(b) after deformation

Fig 17 Bright field TEM micrographs of martensite in splat-quenched Fe-W-C with 6.3wt%W and 0.21wt%C.

Fig 18 δ-ferrite cells with peritectic austenite and M_6C in the cell boundaries: (a) SEM micrograph of splat quenched Fe-W-C with 23wt%W, 0.75%C; (b) STEM micrograph of the same area as (a); (c) SEM micrograph of splat-quenched T1; (d) STEM micrograph of the same area as (c).

Fig 19 XRD traces of (a) splat-quenched and solid-state quenched Fe-W-C alloys; (b) splat-quenched and solid-state quenched T1; (c) splat-quenched and solid-state quenched M2; (d) splat-quenched and solid-state quenched M42.

Fig 20 Isothermal tempering of splat-quenched Fe-6.3wt%W -0.21wt%C: (a) and (b) TEM of Widmanstatten Fe_3C after ~40 mins; (b) hardening response in splat-quenched and solid-state quenched specimens.

Fig 21 Isochronal hardening response in splat-quenched and solid-state quenched steels: (a) Fe-23wt%W - 0.75wt%C; (b) T1; (c) M2; (d) M42.

Fig 22 Peak hardness microstructure in splat-quenched Fe-23wt%W-0.75wt%C; (a) bright field and (b) dark field TEM of M_6C carbide precipitated within δ-ferrite cells.

Fig 23 Peak hardness microstructure in splat-quenched T1; (a) bright TEM of mottled W_2C precipitate within δ-ferrite cells; (b) diffraction pattern and (c) diffraction analysis of area in (a) showing streaks caused by the fine scale W_2C precipitate.

References

1. R.W. Cahn, K.D. Krishnanand, M. Laridjani, M. Greenholz and R. Hill, "2nd International Conference on Rapidly Quenched Metals" Vol II, ed N.J. Grant & B.C. Giessen (Elsevier, 1976) p83.

2. M.J. Bibby and J. Gordon-Parr, J.I.S.I. 202 (1964) 100; and F. Duflos + B. Cantor "Rapidly Quenched Metals III" ed B. Cantor (Metals Society, London 1978) Vol I, p110.

3. J. Bletry, J. Phys. D: Appl Phys 6 (1973) 256.

4. R.E. Cech & D. Turnbull, TMS-AIME 206 (1956) 124.

5. M.G. Scott, J.Mat.Sci., 13 (1978) 291.

6. J.L. Walter, S.F. Bartram and R.R. Russell, Met.Trans, 9A (1978)803

7. W.B. Pearson, "Handbook of Lattice Spacings and Structures of Metals and Alloys", Pergamon, Oxford (1958).

8. U. Koster and U. Herold, Scripta Met; 12 (1978) 75.

9. P.G. Boswell and G.A. Chadwick, Scripta Met., 10(1976) 509.

10. D.H. Avery & W.A. Backofen, Trans. ASM 58 (1965) 551.

11. H.E. Cline & T.H. Alden, TMS-AIME 239 (1967) 710.

12. H.E. Cline & J.D. Livingston, TMS-AIME 245 (1969) 1987.

13. I.R. Sare, Ph.D. thesis, Univ. of Cambridge (1975); T. Arai & N. Kumatsu. JISI Japan 58 (1972) 899; J. Niewiarowski & H. Matyja "Rapidly Quenched Metals III" ed B. Cantor (Metals Soc. London, 1978).

14. S. Takeda, Tech. Rep. Tohoku Univ. 10 (1931) 42; and G. Hobson & D.S. Tyas, Metals and Materials (1968) 144.

15. A.T. Davenport & R.W.K. Honeycombe, Met.Sci.Jnl. 9 (1975) 201.

Martensite Content (%)	Microhardness (kg mm^{-2})	Ferrite grain size/martensite packet size (μm)	Martensite plate dimensions (μm)	
			Width	Length
100	696 ± 55	3.3	0.4	4.0
∿90	585 ± 56	3.6	0.3-0.5	-
90-100	579 ± 48	2.4	0.2	2.0
80	532 ± 28	2.4	0.3-0.5	-
∿80	436 ± 10	3.5	0.3-0.5	3.5
60-80	397 ± 15	4.5	0.3-0.6	6.8
40-80	379 ± 14	3.7	0.5	5.0
50-75	307 ± 12	3.5	0.2-0.5	4.0
20-60	297 ± 18	2.6		
<60	272 ± 5	3.8		
0	263 ± 12	6.0		
0	259 ± 21	3.4		
0	242 ± 7	4.0		
0	227 ± 16	5.0		

Table 1: Microhardness and microstructural parameters for some of the splat-quenched pure iron specimens.

wt%Ni or Mn	Phases Present					
	Fe-Ni		Fe-Ni-C		Fe-Mn	
	Splat-quenched	Solid-State quenched	Splat-quenched	Solid-state quenched	Splat-quenched	Solid-state quenched
0	α	α	α	α	α	α
5	α	α	α	α	α	α
10	α	α	α	α	$\alpha + (\gamma)$	α
15	α	α	α	α	$\alpha + \gamma + (\varepsilon)$	$\alpha + \varepsilon$
20	$\alpha + \gamma$	α	α	α	$\gamma + (\varepsilon)$	$\alpha + \gamma + \varepsilon$
25	γ	α	γ	$\alpha + (\gamma)$		
30	γ	$\alpha + \gamma$	γ	$(\alpha) + \gamma$		
35	γ	γ	γ	γ		
40	γ	γ	γ	γ		

Table 2: X-ray diffractometer results showing phases present in splat-quenched and solid-state quenched Fe-Ni, Fe-Ni-C, and Fe-Mn alloys. Phases in brackets were present in traces only.

thickness (μm)	testing temperature T(K)	strain rate sensitivity m	correlation coefficient r	$\log_{10} K_3$
31 ± 2	297	.48	.995	1.86
44 ± 4	297	.42	.998	1.68
	312	.42	.999	1.48
	328	.45	.998	1.43
	334	.45	.997	1.38
	348	.43	.997	1.12
	368	.40	.995	0.87
54 ± 4	297	.40	.996	1.57
58 ± 2	297	.40	.993	1.58
63 ± 3	297	.41	.997	1.63
75 ± 6	297	.40	.999	1.56
	310	.43	.999	1.49
	319	.43	.999	1.36
	324	.42	.998	1.31
	329	.43	.998	1.32
	339	.46	.997	1.31
	342	.45	.997	1.17
	349	.42	.996	1.05
	359	.47	.998	1.06
80 ± 4	297	.42	.994	1.64
92 ± 5	297	.41	.995	1.59
118 ± 11	297	.44	.994	1.64
all specimens, T = 297K		.42	.979	1.63
$\bar{m}$, T = 297K		.42 ± .02		
$\bar{m}$, T > 297K		.43 ± .02		
$\bar{m}$, all specimens		.43 ± .02		

TABLE 3: Strain rate sensitivity of melt-spun Pb-Sn eutectic tapes as a function of tape thickness and testing temperature

Strain rate $\dot{\varepsilon}$ (s^{-1})	Activation energy for superplastic flow Q, (kJ mole $^{-1}$)			correlation coefficient, r		
	44μm thick tape	75μm thick tape	both 44 and 75μm thick tape	44μm thick tape	75μm thick tape	both 44 and 75μm thick tape
1.2×10^{-5}		56			.989	
2.3×10^{-5}	49	57	53	.998	.983	.971
5.9×10^{-5}	52	59	56	.998	.983	.981
1.2×10^{-4}	55	58	57	.999	.986	.982
2.3×10^{-4}	54	56	55	.999	.990	.984
5.6×10^{-4}	50	52	50	.997	.990	.985
1.0×10^{-3}		50			.989	
2.1×10^{-3}		49			.975	
$\bar{Q}$ all specimens			54 ± 3			

TABLE 4: Activation energy for superplastic flow in melt-spun Pb-Sn eutectic tapes as a function of tape thickness amd strain rate.

thickness (μm)	grain size, d(μm)		
	as solidified top surface	as solidified bottom surface	as-deformed
31 ± 2	4.1 ± 1.0	4.2 ± 1.2	2.9 ± 0.6
44 ± 4	3.9 ± 1.0	3.8 ± 0.7	—
54 ± 4	3.9 ± 0.8	3.8 ± 0.8	2.6 ± 0.5
63 ± 3	4.0 ± 0.9	3.3 ± 0.8	—
75 ± 6	4.4 ± 1.2	3.8 ± 1.1	3.5 ± 0.9
80 ± 4	4.0 ± 1.0	4.3 ± 1.0	2.8 ± 0.6
92 ± 5	3.9 ± 1.3	3.6 ± 1.2	2.9 ± 0.7
116 ± 11	4.0 ± 1.0	3.7 ± 1.2	3.2 ± 0.4
$\bar{d}$ (all specimens)	4.0	3.8	3.0

TABLE 5: Grain size in melt-spun Pb-Sn eutectic tapes as a function of tape thickness. The top surface is the surface not in contact with the rotating copper drum during solidification. Each grain size was determined as the mean of 30 measurements of the number of grain intersections along a 3μm line using micrographs such as figures 4 and 5. Scatter bands are given as ± one standard deviation.

Alloy	C	W	Mo	Cr	V	Co
FeWC1	0.21	6.3				
FeWC2	0.31	9.5				
FeWC3	0.42	13.0				
FeWC4	0.54	16.5				
FeWC5	0.65	20.0				
FeWC6	0.75	23.0				
T1	0.75	18.0		4.0	1.0	
M2	0.85	6.0	5.0	4.0	2.0	
M42	1.10	1.50	9.5	3.75	1.15	8.0
M42 (powder)	1.03	1.59	9.80	4.35	1.08	8.0

Table 6: Nominal compositions of ternary Fe-W-C alloys and AlSl classifications of M2, M42 and Tl tool steels used for splat-quenching and plasma-spraying (compositions in wt%; in all cases the balance is Fe).

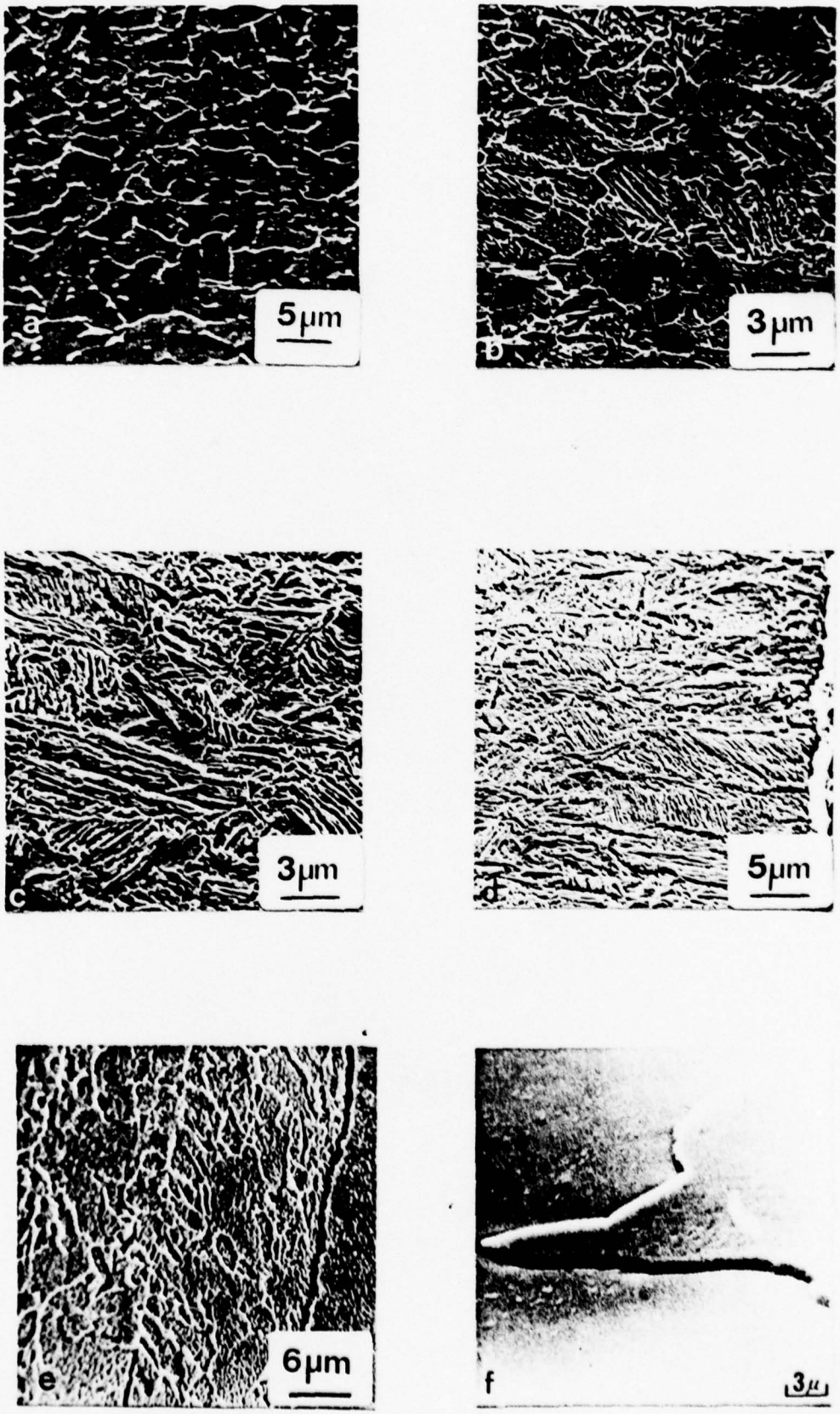

Figure 1

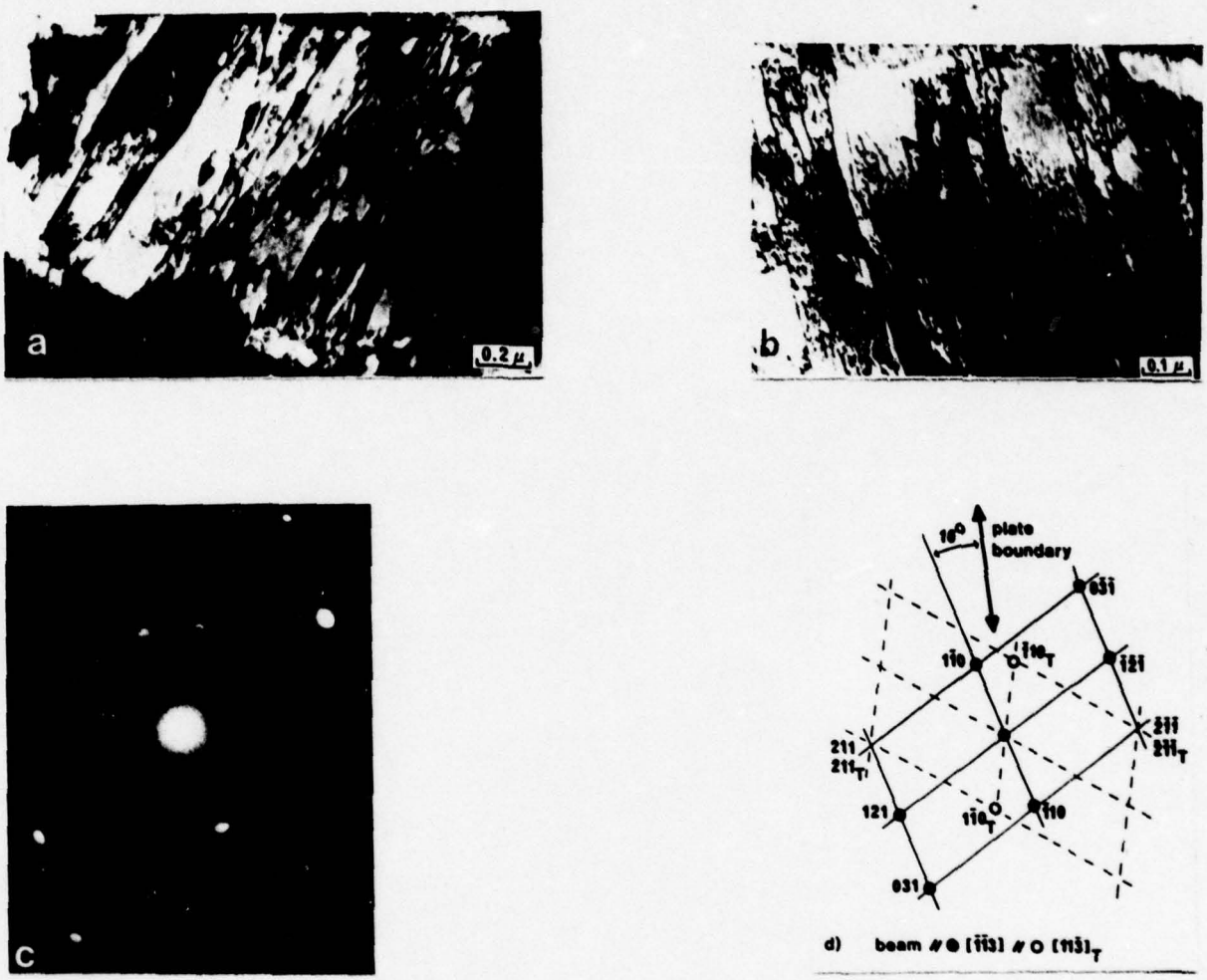

Figure 2

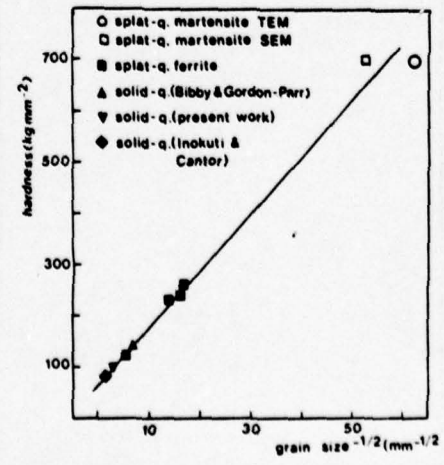

Figure 3

a

b

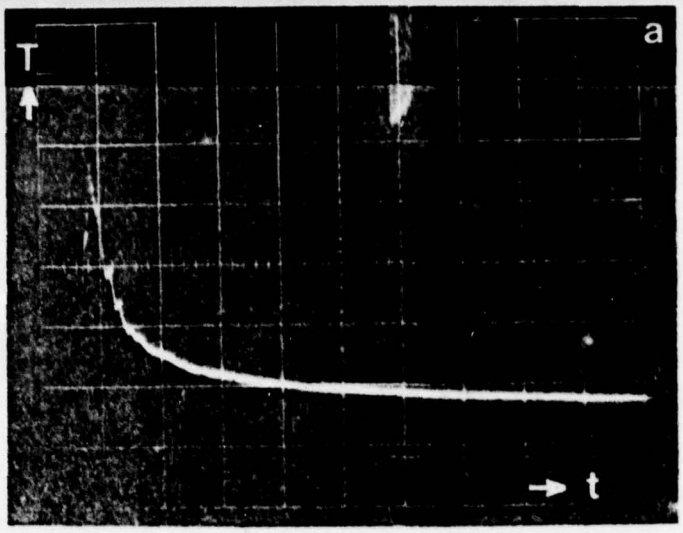
T
a
t

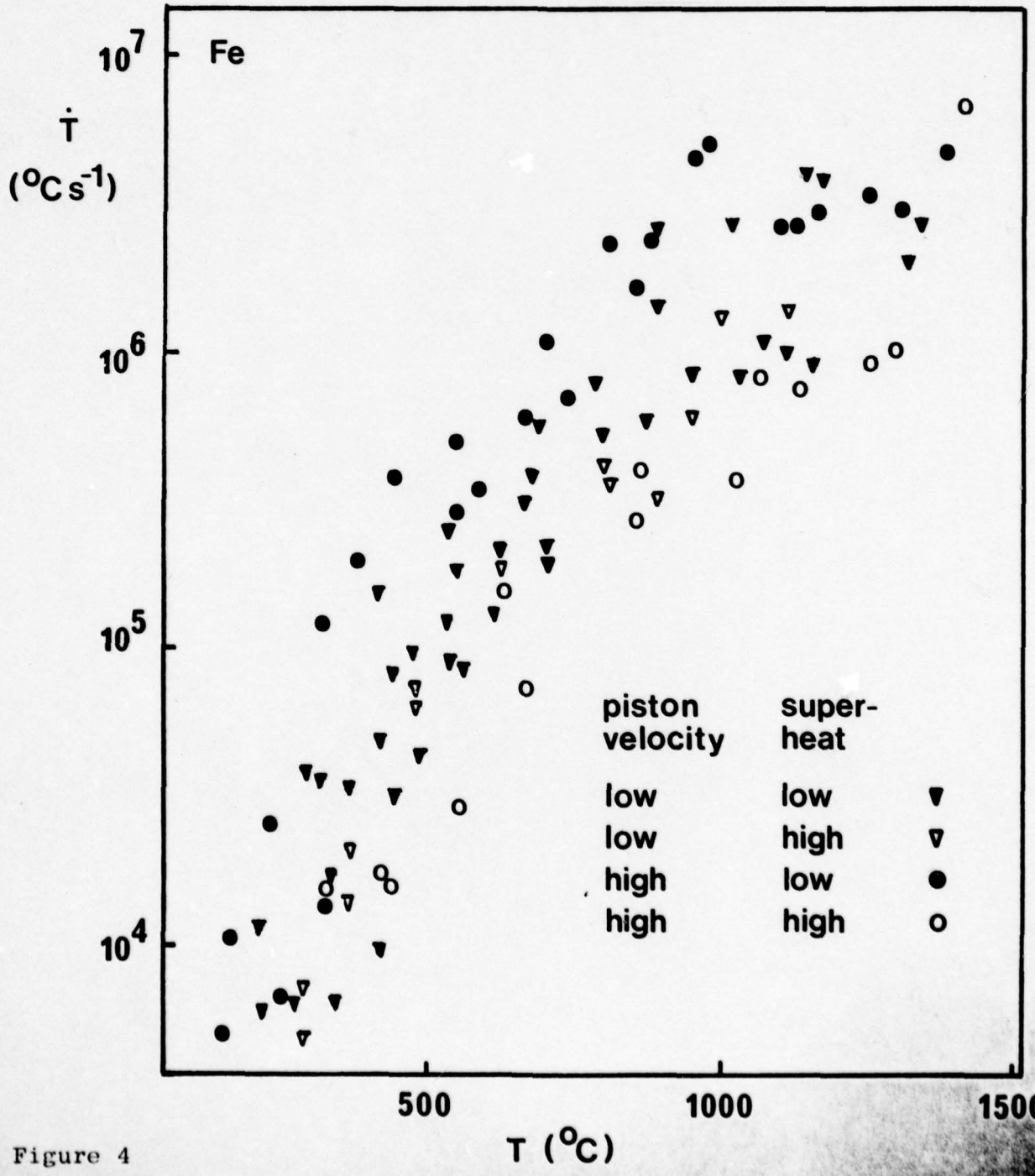
Fe
10^7
10^6
10^5
10^4
$\dot{T}$
($^oC\,s^{-1}$)
piston velocity
super-heat
low low
low high
high low
high high
500
1000
1500
T (^oC)

Figure 4

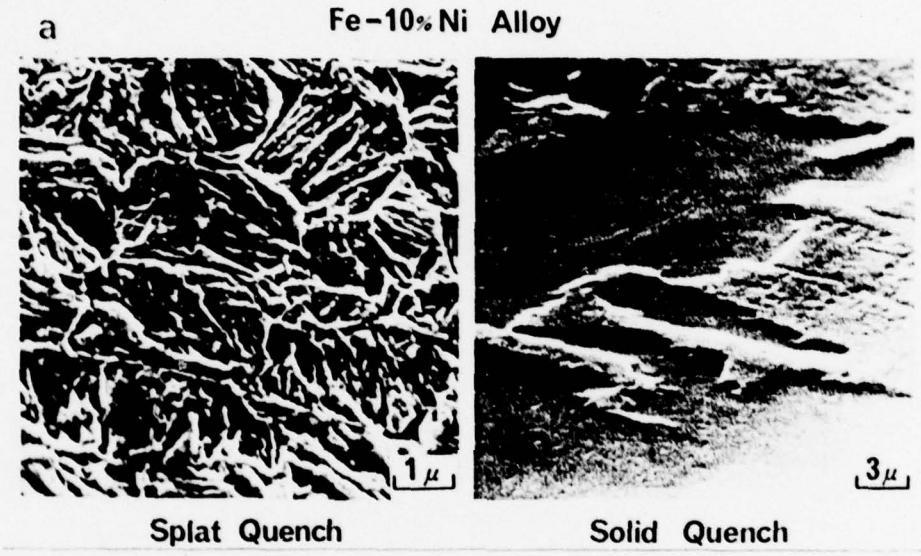

Figure 5 a

b

Fe–30%Ni Alloy

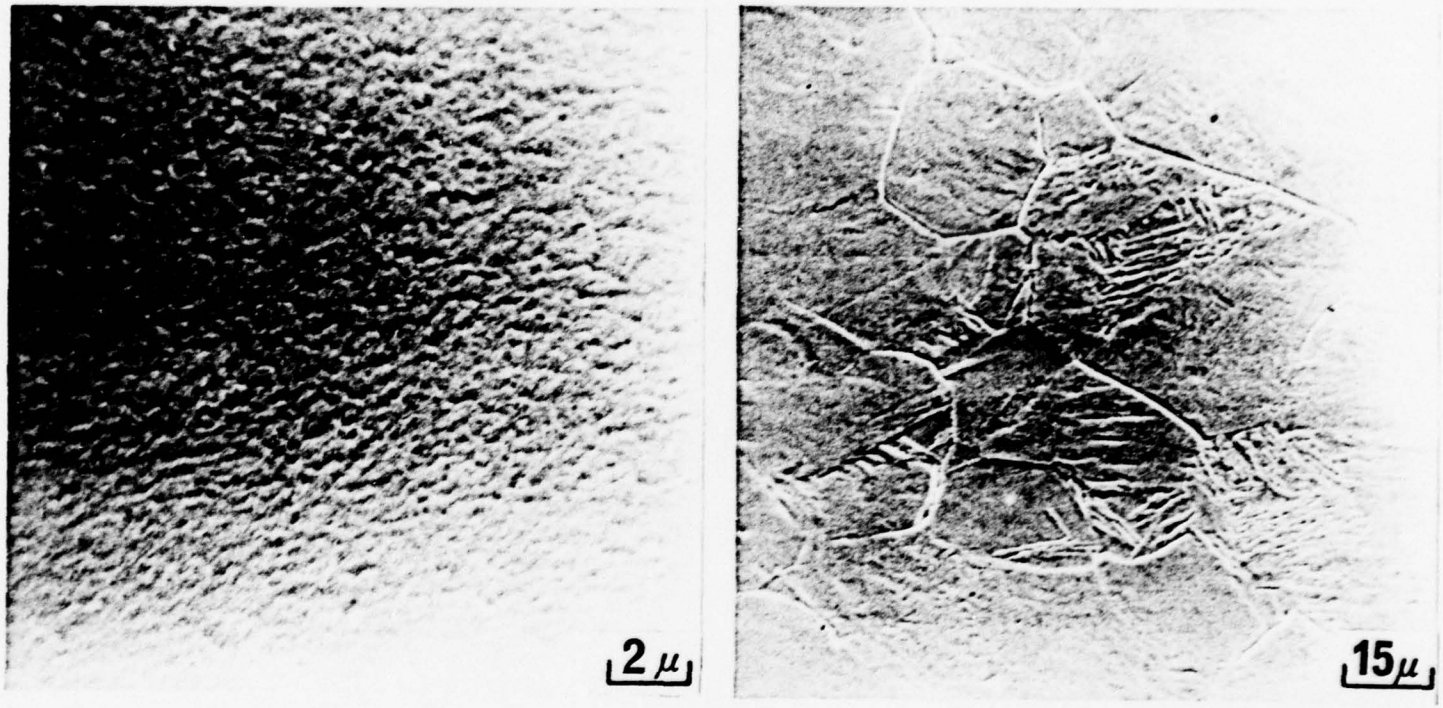

Splat Quench

Solid Quench

Figure 5 b

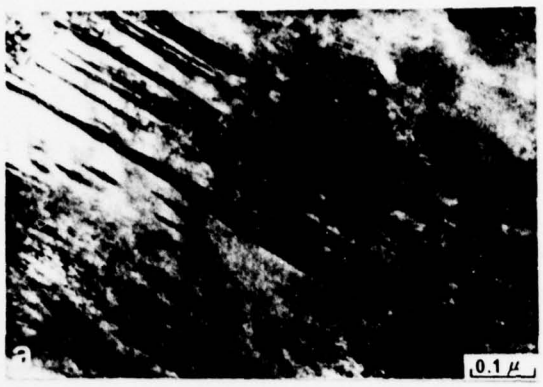
a
0.1 μ

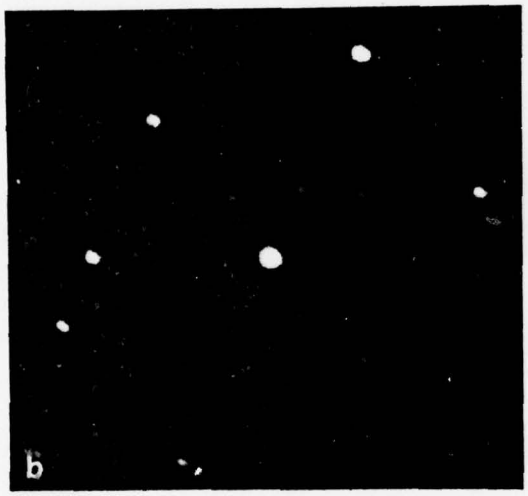
b

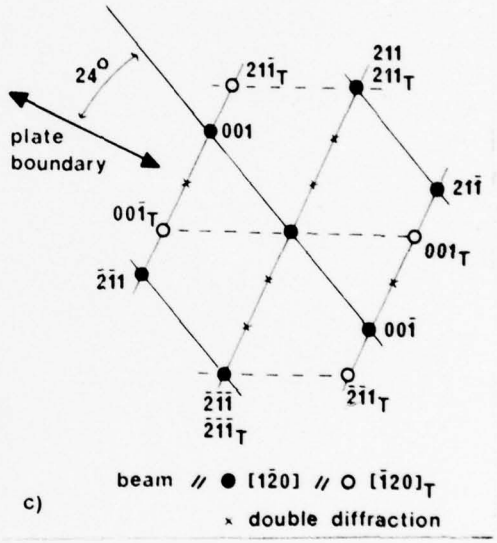
24°
plate
boundary
211̄T
211
211T
001
21̄1̄
001̄T
001T
2̄11
001̄
2̄1̄1̄
2̄11T
2̄1̄1̄
2̄11̄T
beam // ● [1$\bar{2}$0] // ○ [$\bar{1}$20]T
× double diffraction
c)


d
0.2 μ


e

Figure 6

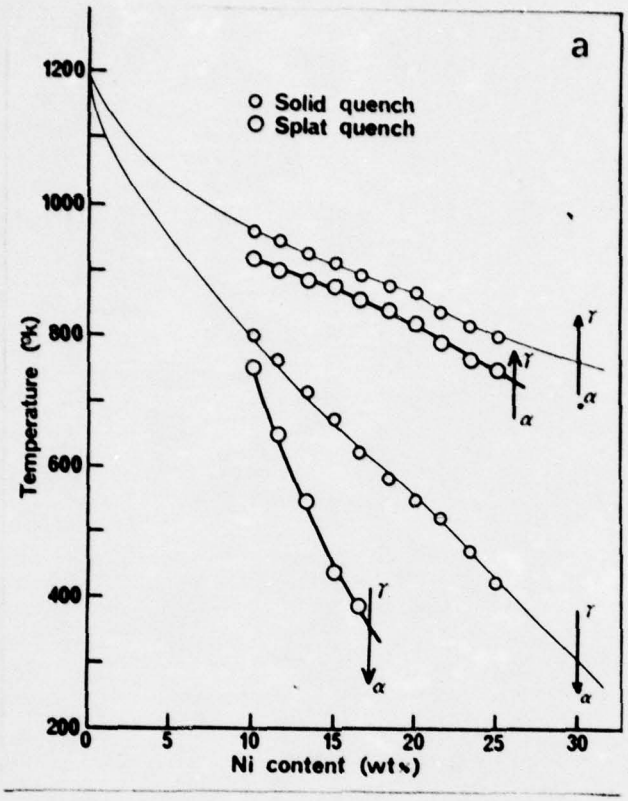

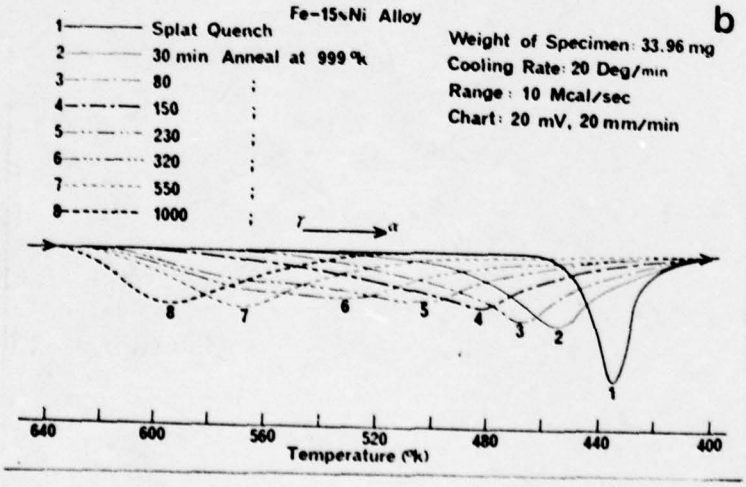

Figure 7 a and b

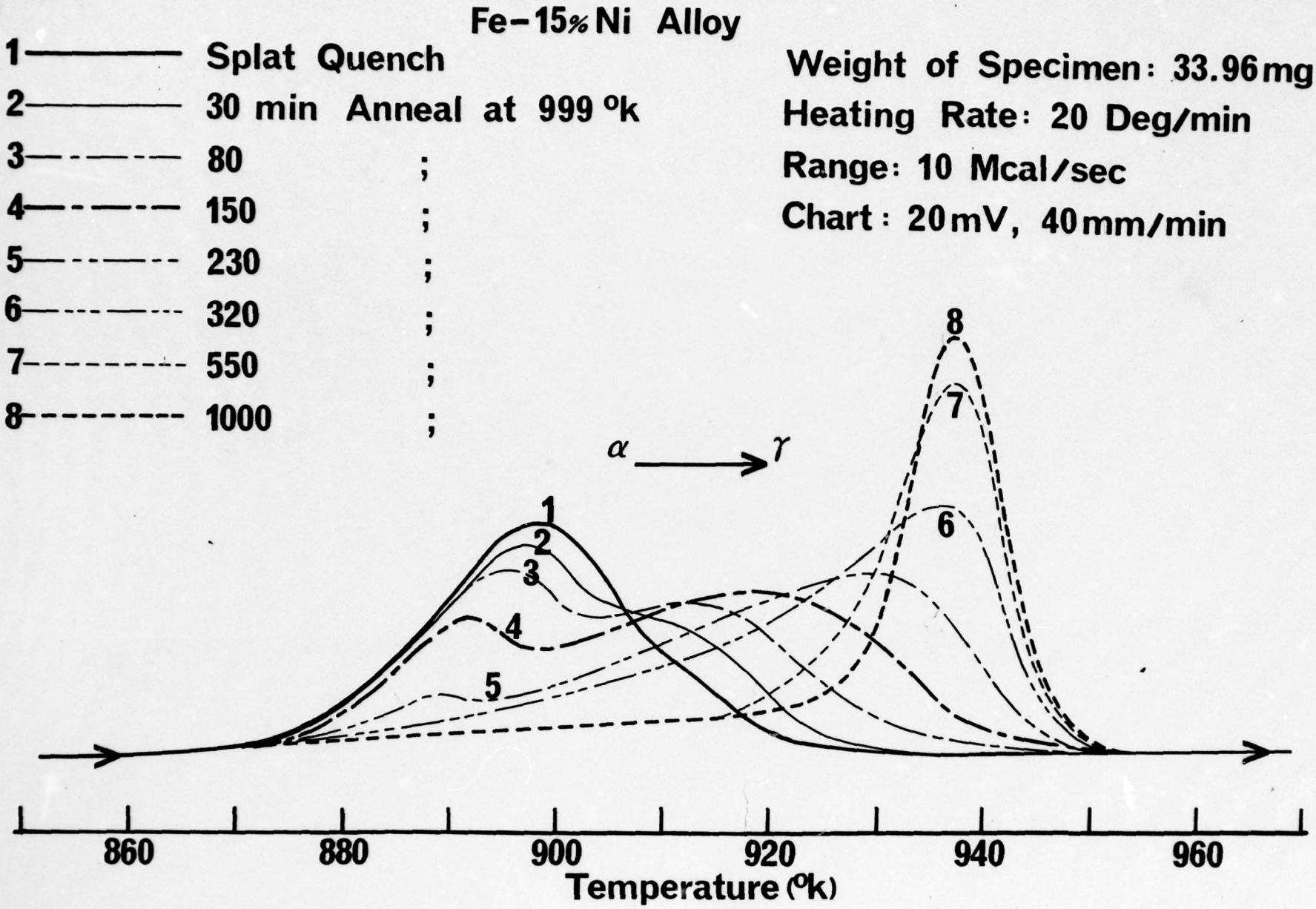
Fe-15% Ni Alloy
1 Splat Quench
2 30 min Anneal at 999 °k
3 80 ;
4 150 ;
5 230 ;
6 320 ;
7 550 ;
8 1000 ;
Weight of Specimen: 33.96 mg
Heating Rate: 20 Deg/min
Range: 10 Mcal/sec
Chart: 20 mV, 40 mm/min
α → γ
860
880
900
920
940
960
Temperature (°k)

Figure 7 c

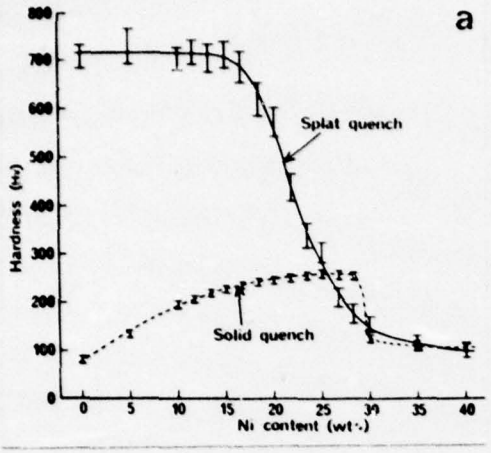
a
Splat quench
Solid quench
Hardness (Hv)
Ni content (wt%)

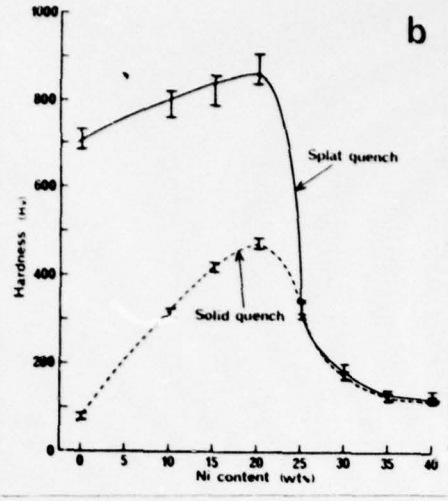
b
Splat quench
Solid quench
Ni content (wt%)

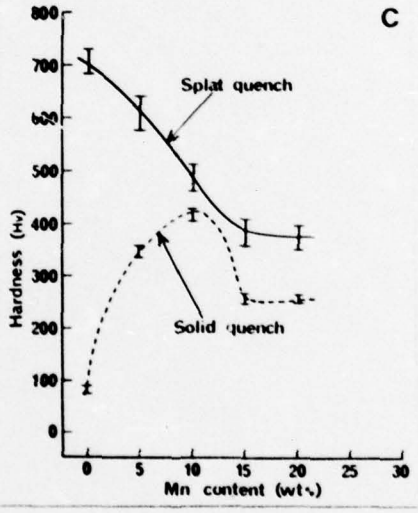
c
Splat quench
Solid quench
Hardness (Hv)
Mn content (wt%)

Figure 8

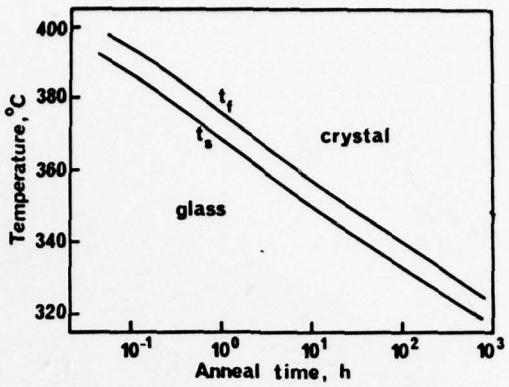

Figure 9

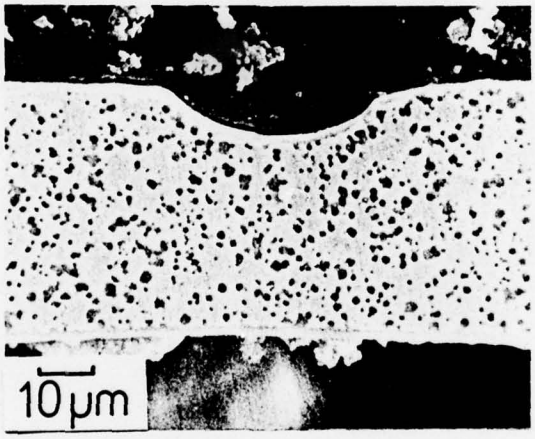

Figure 10

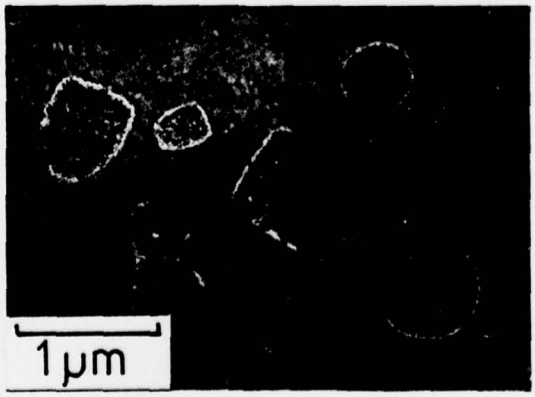

Figure 11

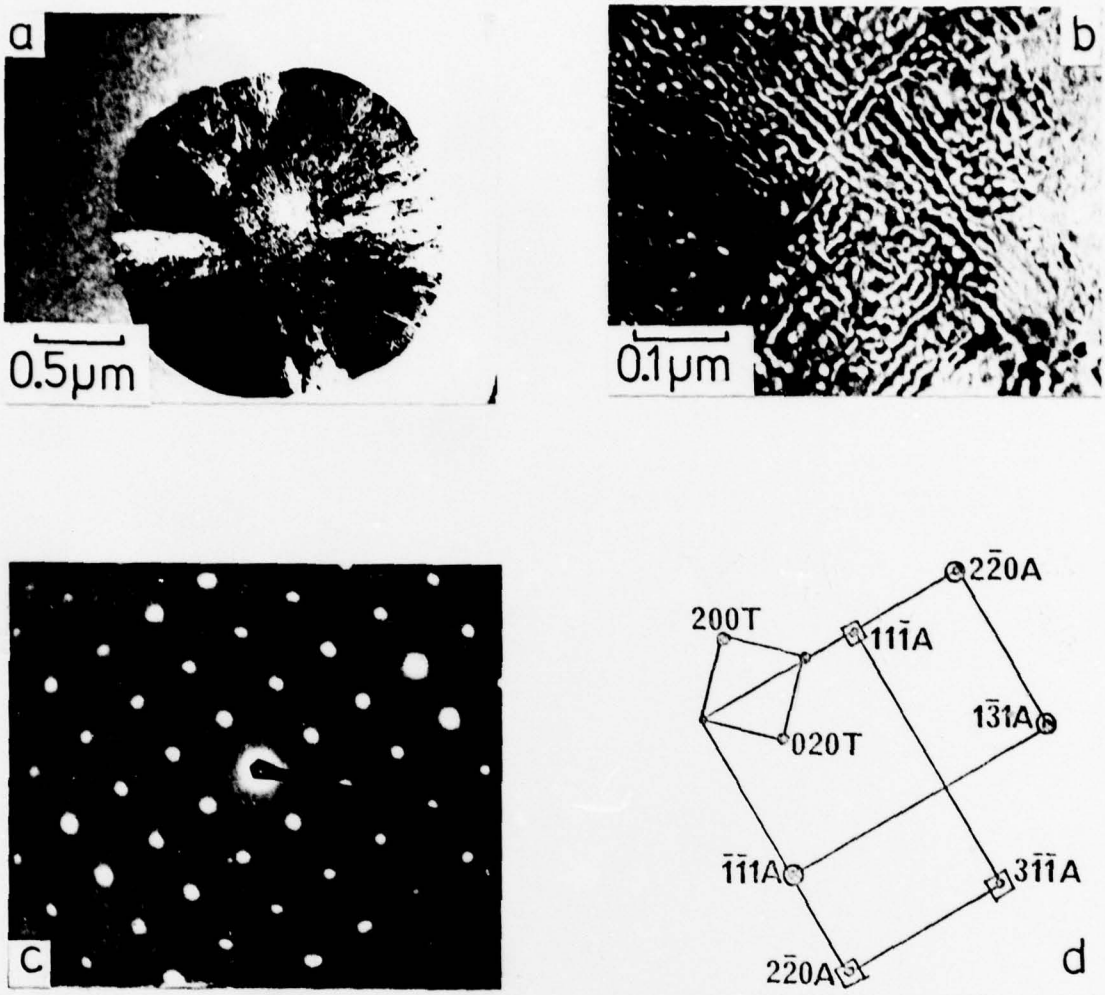

Figure 12

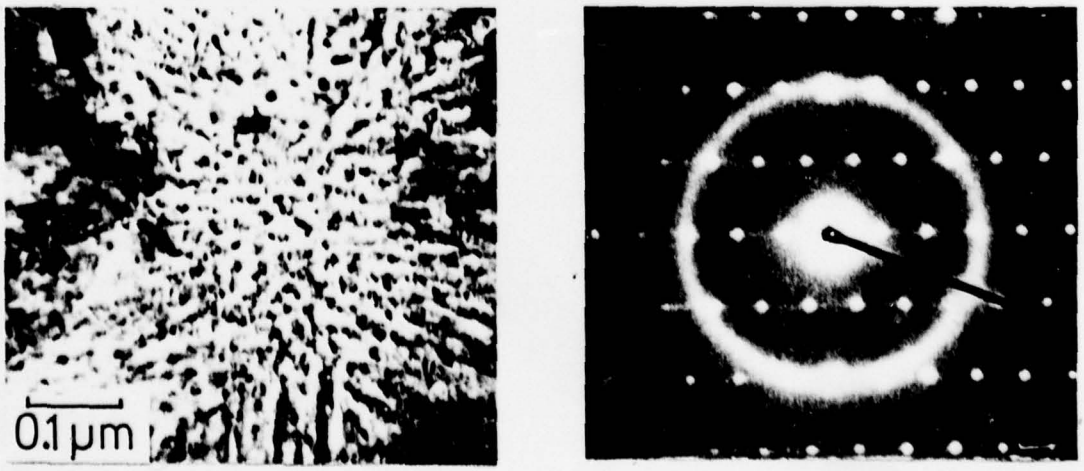

Figure 13

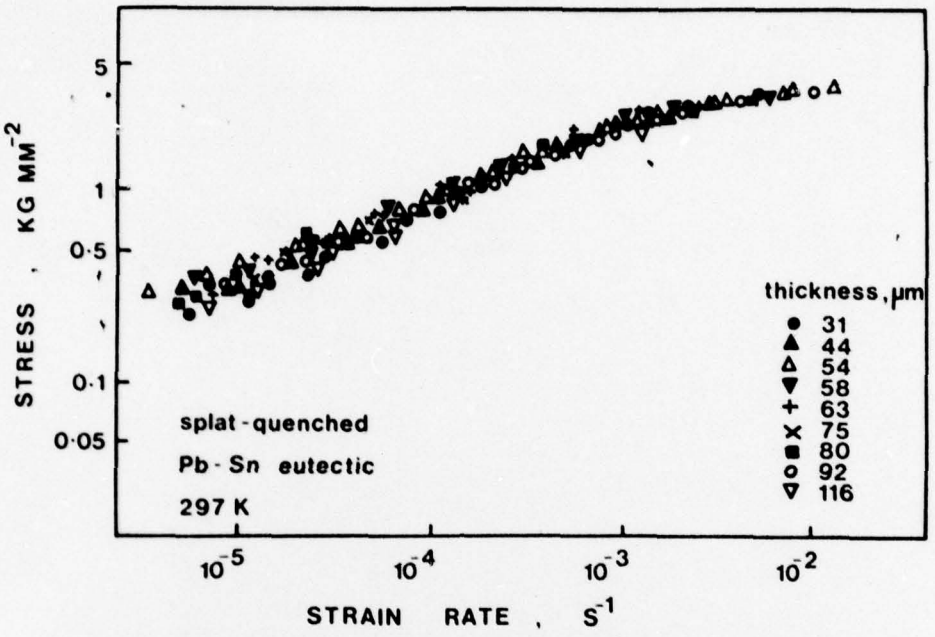

Figure 14

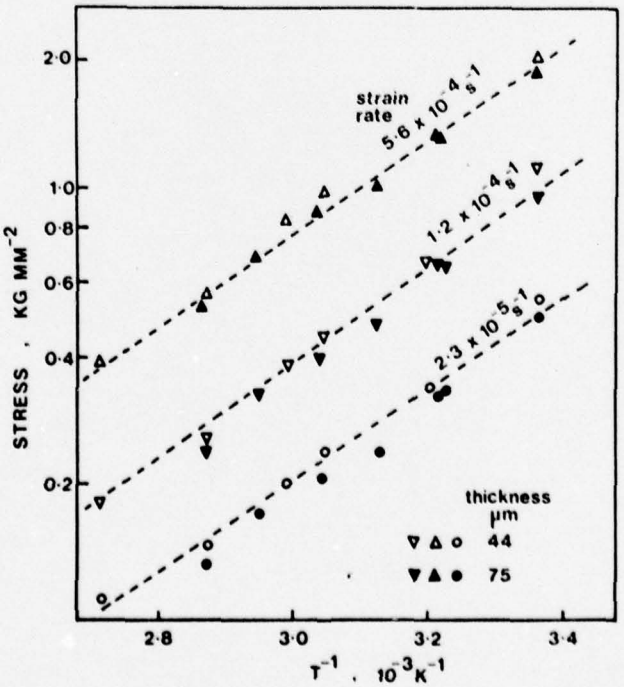

Figure 15

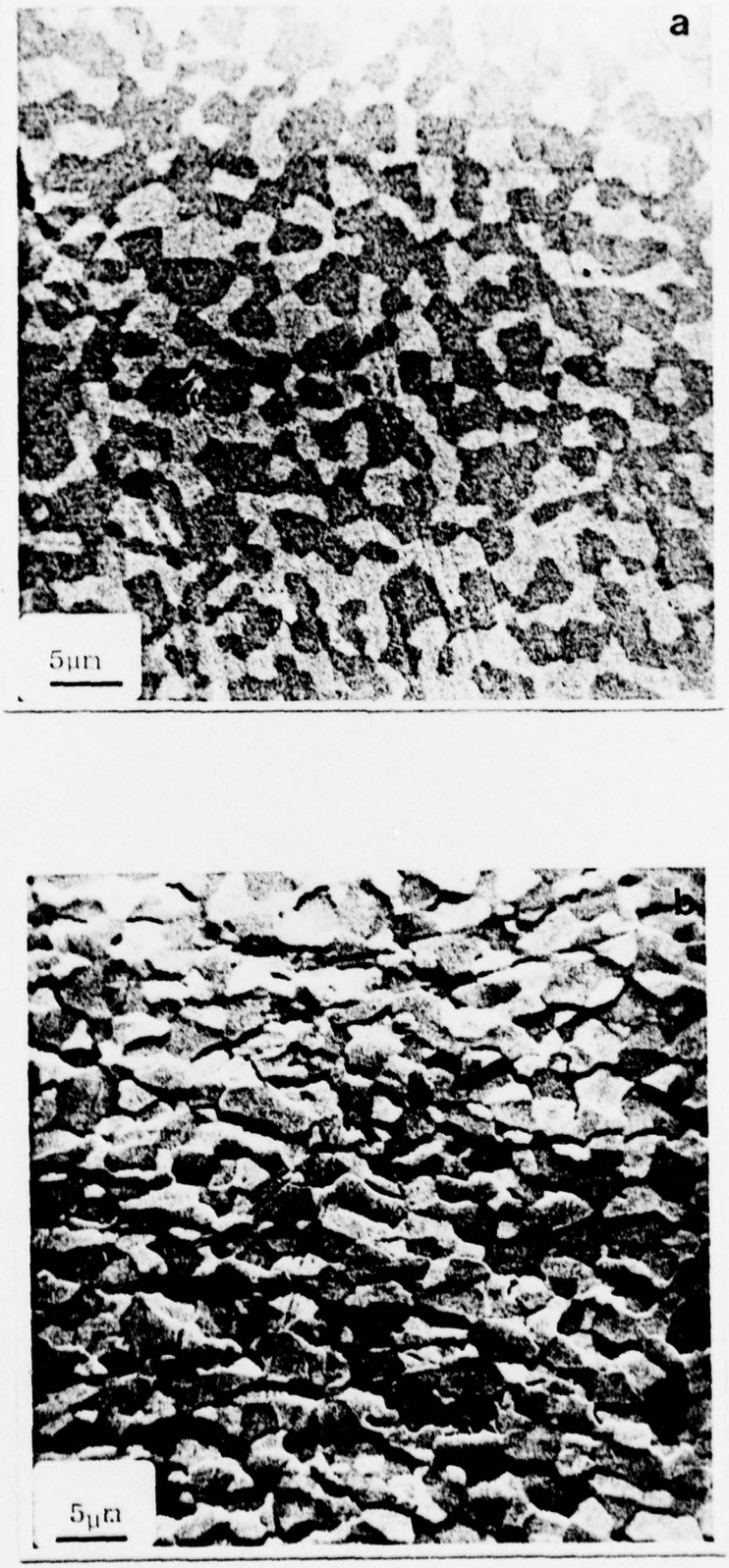

Figure 16

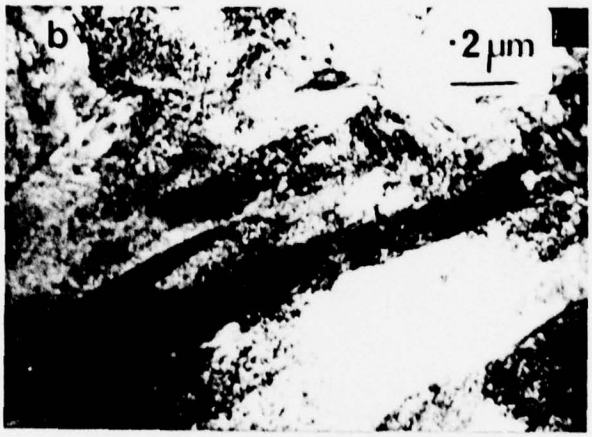

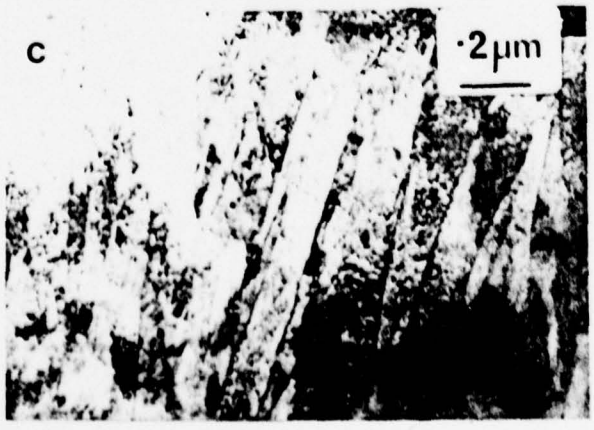

Figure 17

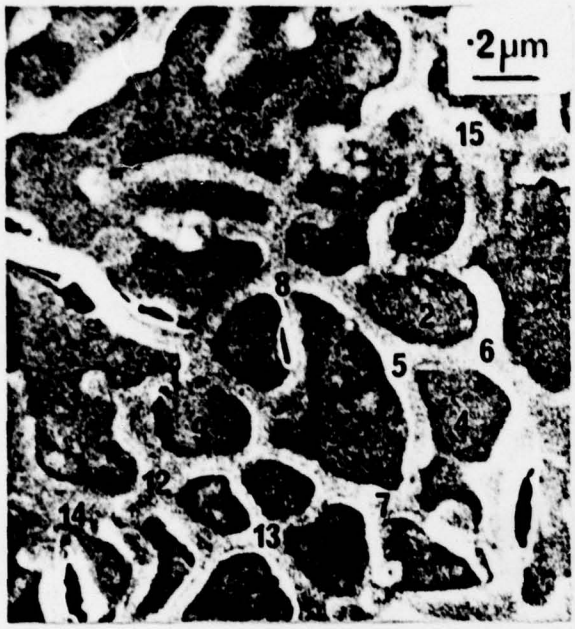

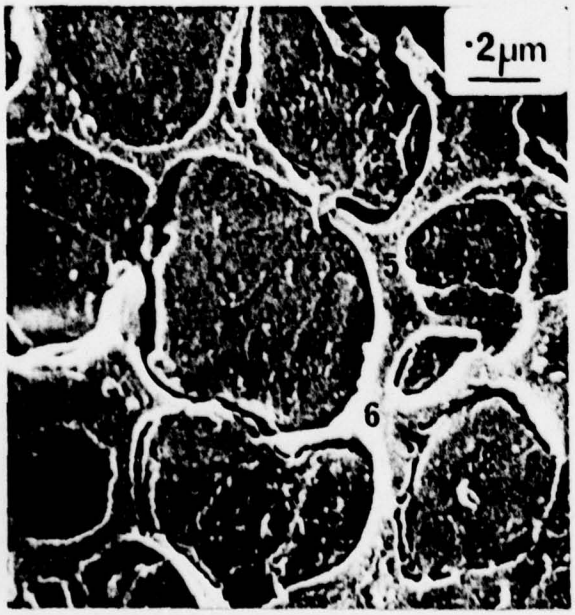

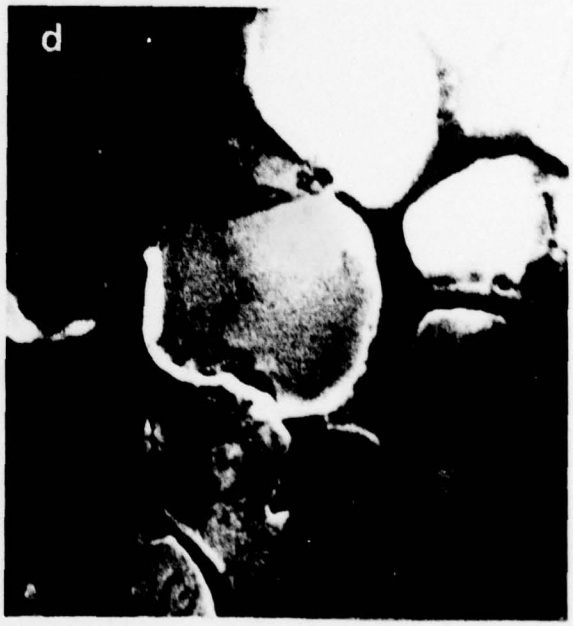

Figure 18

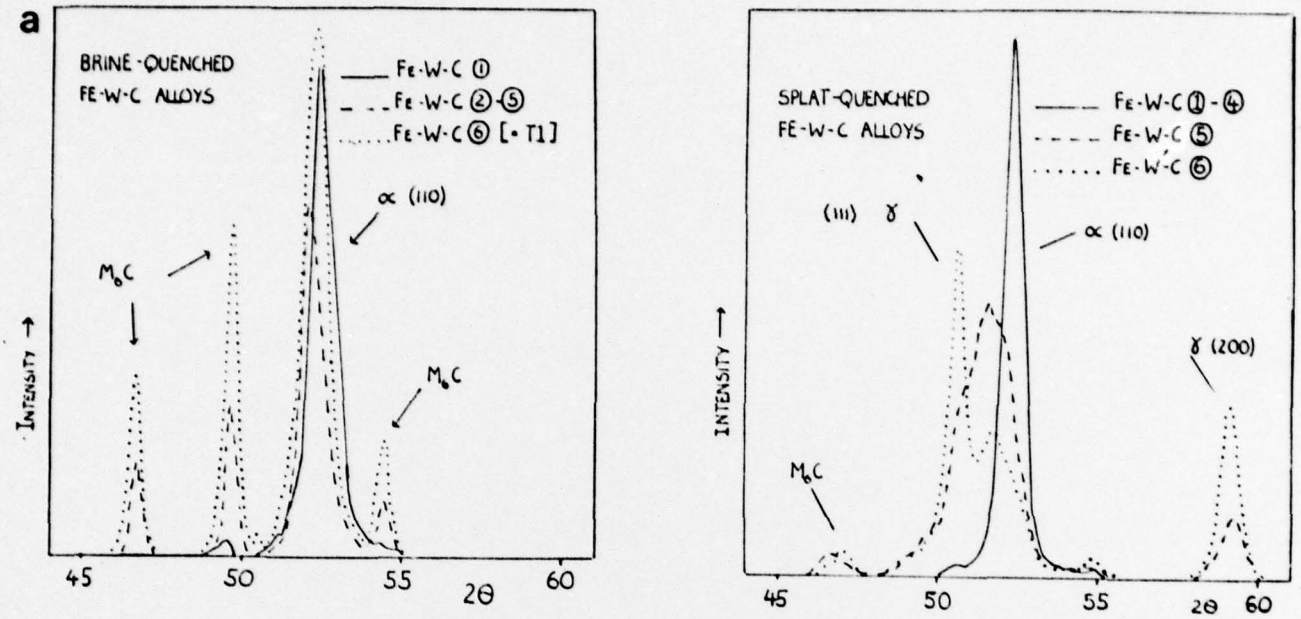

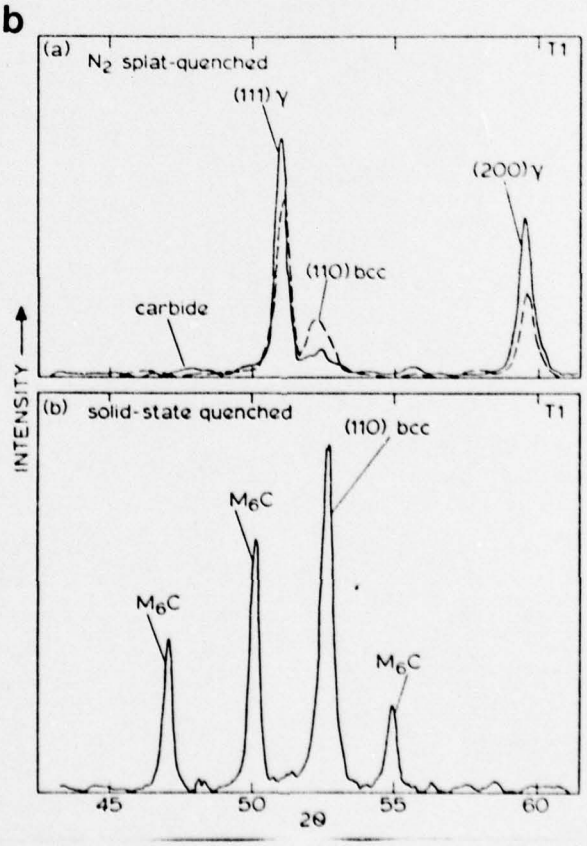

Figure 19 a and b

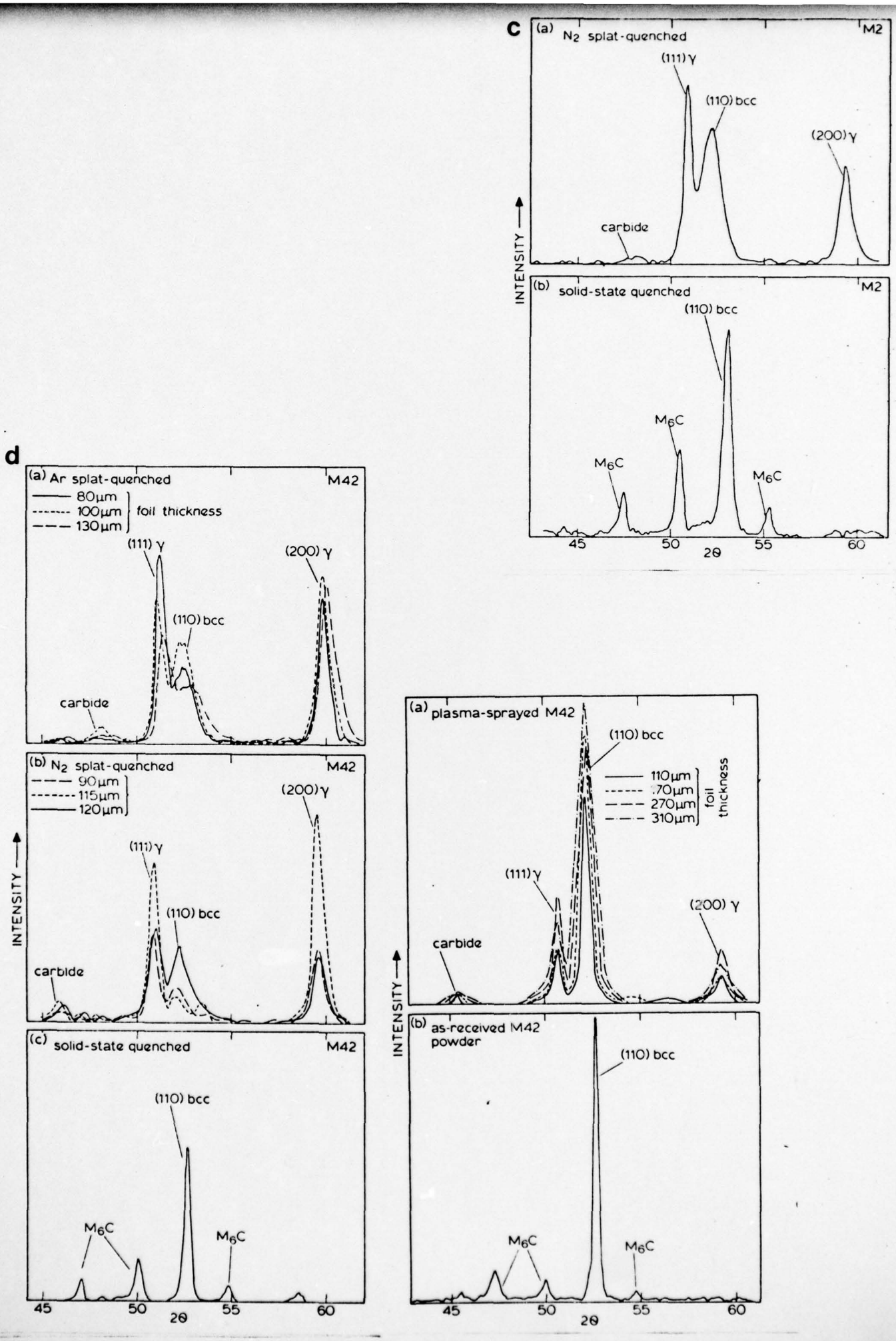

Figure 19 c and d


a
·7μm


b
·5μm

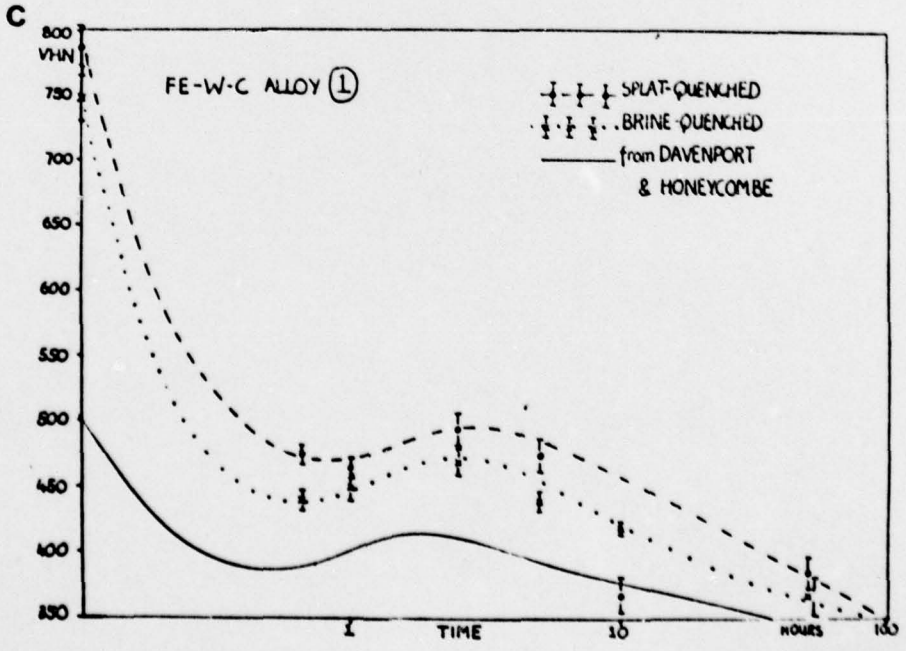
c
800
VHN
750
700
650
600
550
500
450
400
350
FE-W-C ALLOY (1)
SPLAT-QUENCHED
BRINE-QUENCHED
from DAVENPORT
& HONEYCOMBE
1
TIME
10
HOURS
100

Figure 20

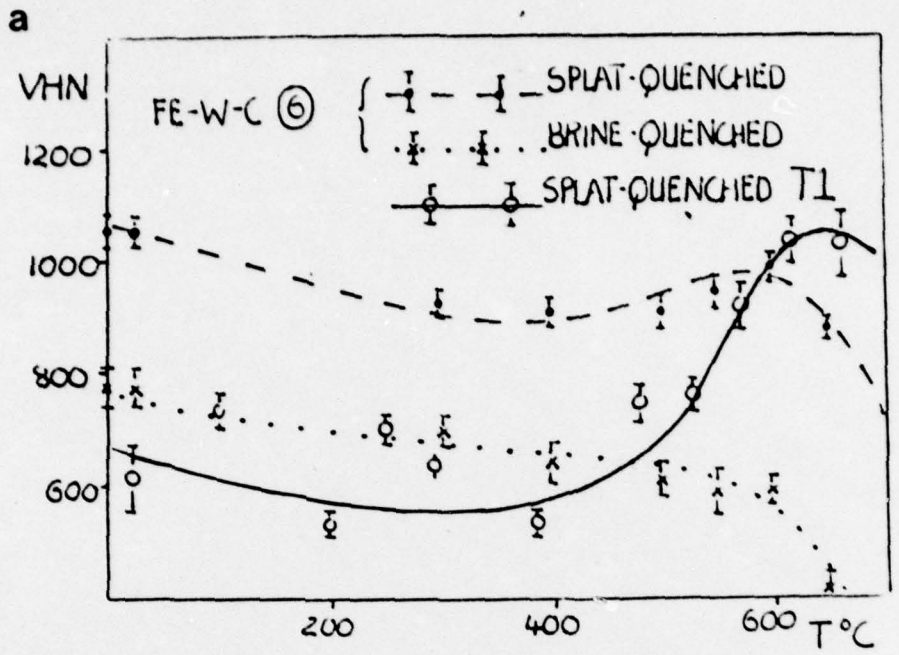
a
VHN
FE-W-C ⑥
SPLAT-QUENCHED
BRINE-QUENCHED
SPLAT-QUENCHED T1
1200
1000
800
600
200
400
600
T°C

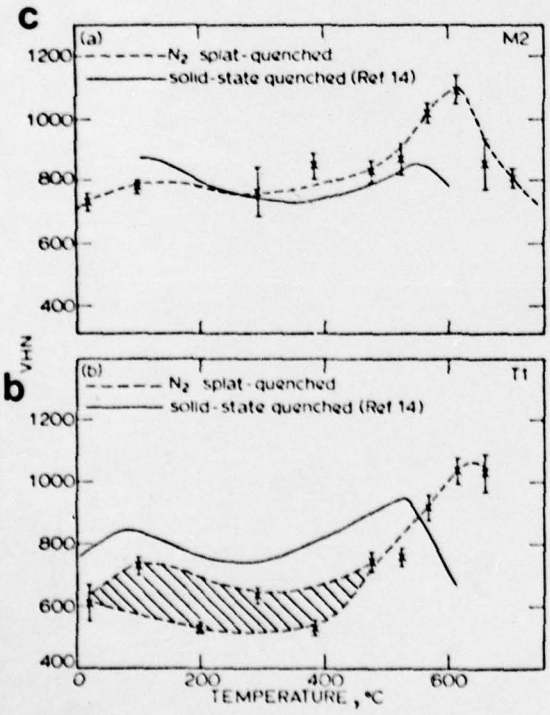
c
(a)
M2
N2 splat-quenched
solid-state quenched (Ref 14)
1200
1000
800
600
400
b
VHN
(b)
T1
N2 splat-quenched
solid-state quenched (Ref 14)
1200
1000
800
600
400
0
200
400
600
TEMPERATURE, °C

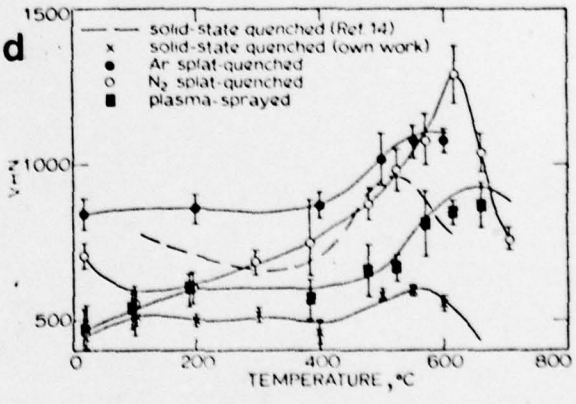
d
solid-state quenched (Ref 14)
solid-state quenched (own work)
Ar splat-quenched
N2 splat-quenched
plasma-sprayed
1500
1000
500
0
200
400
600
800
TEMPERATURE, °C

Figure 21

Figure 22

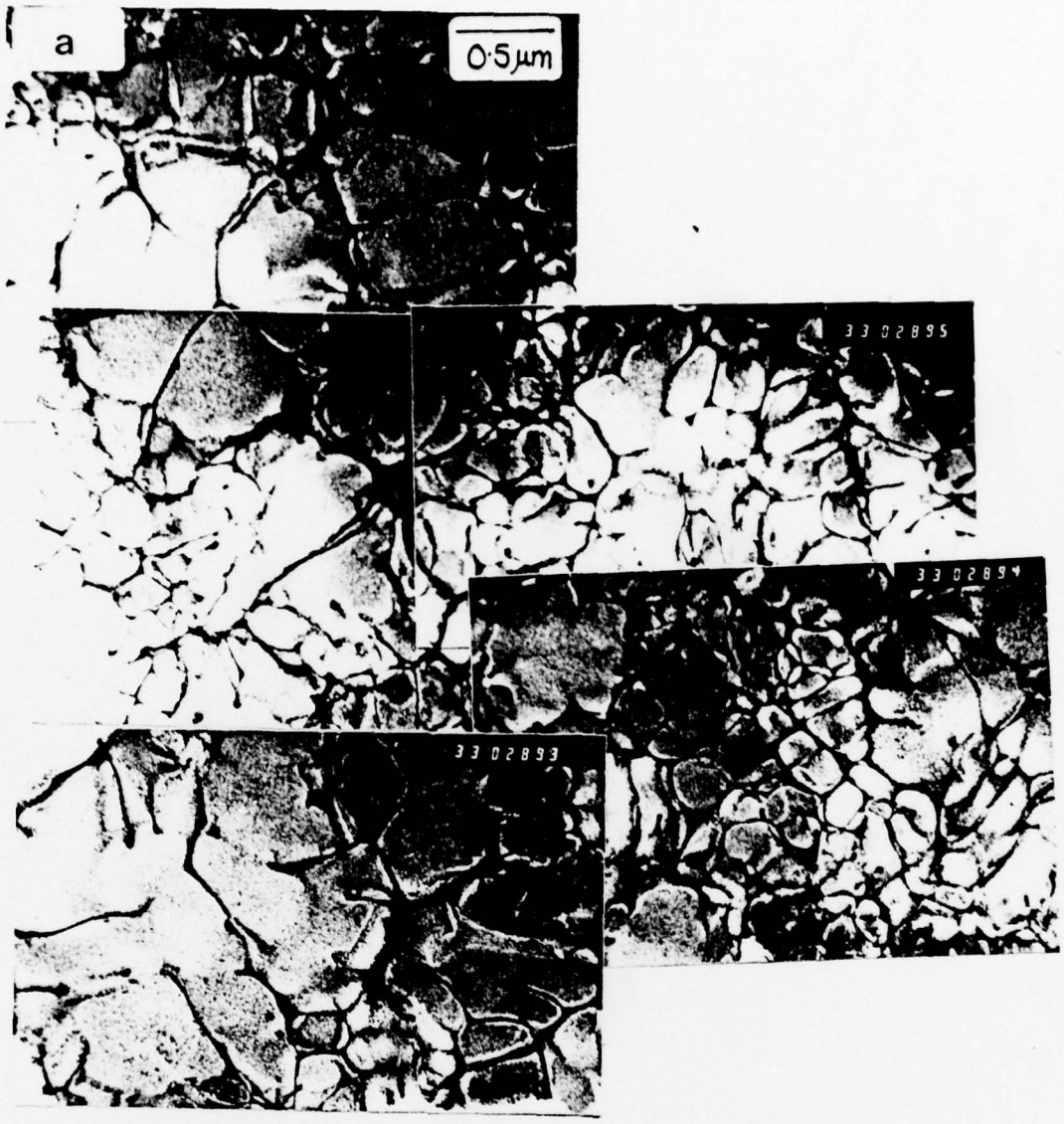
a
0·5μm
33 02895
33 02894
33 02893


b

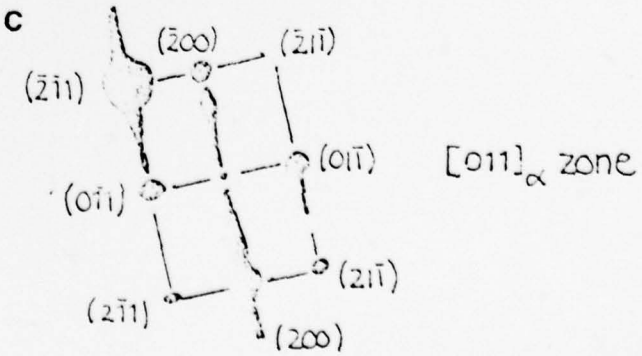
c
(2̄00)
(2̄1̄1)
(01̄1̄)
(01̄1)
(21̄1̄)
(2̄11)
(200)
[011]α zone

Figure 23